平成１２年度　分子科学研究所研究会

「高機能固体レーザーとその応用（２）」

― The Art of Solid-State Lasers and Nonlinear Frequency Conversion Devices ―

主催：分子科学研究所

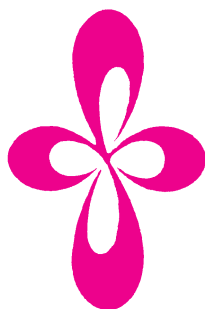Organized by Institute for Molecular Science

共催：電気学会

In Cooperation with the Institute of Electrical Engineers of Japan

協賛：レーザー学会

Approved by the Laser Society of Japan

岡崎国立共同研究機構岡崎コンファレンスセンター

OKAZAKI Conference Center, OKAZAKI National Research Institutes

平成 12 年 10 月 12 日

平成１２年度　分子科学研究所研究会

「高機能固体レーザーとその応用（２）」
── The Art of Solid-State Lasers and Nonlinear Frequency Conversion Devices ──

ＬＤ励起マイクロチップ固体レーザの物性と応用

大塚　建樹

（東海大学）

Physics and Applications of LD-Pumped Microchip Solid-State Lasers

Kenju Otsuka

(Tokai University)

Abstract

Recent topics and physics inherent in LD-pumped solid-state lasers with microcavity configurations, such as low-frequency coherence created by quantum inteference of lower laser-level atoms, stimulated phonon sideband emissions around $1.55\,\mu$m, and noise-induced chaotic burst generations with feedback, have been reviewed. Highly-sensitive self-mixing laser Doppler vibrometry and velocimetry, as well as stable intracavity SHG have been demonstrated.

キーワード：　マイクロチップレーザ、量子干渉、誘導ラマン発振、量子雑音誘起カオス的バースト、自己光混合レーザドップラー光計測、多重遷移共振器内第二高調波発生

（microchip lasers, quantum interference, quantum-noise-induced chaotic bursting, stimulated Raman emission, self-mixing laser Doppler measurements, multitransition intracavity second-harmonic generation）

1　はじめに

　　筆者らは、１９７４年に開発した直接化合物系レーザ結晶 $LiNdP_4O_{12}(LNP)$[1]を厚さ３００μmの薄片に研磨し、当時出力１０ｍＷ程度であった半導体レーザ（以下、ＬＤと呼ぶ）で端面励起し、１０４８および１０３２nm　の単一縦横モード発振を実現し、現在のＬＤ励起マイクロチップ固体レーザのプロトタイプを得てから２１年経過した[2]。この単色性の極めて優れた光源は、まだ未成熟であったＬＤの代替として、当時、注目されていた長波長帯光ファイバ伝送やコヒーレント光伝送の基礎実験にも用いられた[3]。

　　しかしながら、その後のＬＤの技術革新により、光伝送用光源としての価値は失われた。一方で、ＬＤ励起固体レーザは、堅牢かつ小型の高品位光源として、その特長を生かした多岐にわたる応用が見直され、幾多の固体レーザ材料の合成と相俟って、今や大きなマーケットを形成するに至っている。

　　本報告では、マイクロ共振器構成に直接起因して発現し、旧来の大型固体レーザでは顕在化し得ない効果としての（１）レーザ下準位原子の量子干渉、（２）共振器内フォノン側帯波発光、（３）戻り光誘起不安定現象、などの物性とこれらに起因する非線形ダイナミクスについて述べたい。また、ＬＤ励起マイクロ共

振器ＬＮＰレーザの超高感度レーザドップラー計測および安定な多重遷移緑色レーザへの応用にも言及する。

2　量子干渉効果

Ｎｄに代表される活性原子を含むレーザ材料では、母材の結晶場の相違により、準安定なレーザ上準位と終状態である下準位が多シュタルク分裂の様子が異なり、多様な蛍光スペクトルを示す。一般に、下準位原子の寿命は、数１０～数 100ns であり、[4]　上準位原子の蛍光寿命１００～２００μｓに比べて格段に短く、下準位原子のダイナミクスは断熱消去され、シュタルク分裂した下準位に分布する原子に相関は陽に現われない。

しかしながら、マイクロ共振器を使うＬＤ励起固体レーザにおいては、光子寿命が数 ns ～数１０ps 程度にまで短くなり、共通の上準位から異なる下準位間でレーザ発振が生ずる場合（量子光学でのΛ型遷移）においては、断熱消去は許されず、多重遷移発振光電界のビート波によってシュタルク分裂に対応した低周波のコヒーレンス（**Low Frequency Coherence; LFC**）が形成され、異なる下準位原子間には量子干渉効果によって強い相関が現われる。その結果、誘導吸収が助長され、光強度依存型の非線形な吸収効果がレーザのダイナミックスに劇的な変化をもたらす。

2．1　多重遷移ＬＮＰレーザの反位相パルセーション

ＬｉＮｄＰ$_4$Ｏ$_{12}$**(LNP)** は、Ｎｄを結晶の構成元素としてむ。高Ｎｄ濃度性に直接起因する **LD** 光の非励起領域での共鳴吸収損失と高密度励起時の励起原子間のオージェ再結合よる空間的ホールバーニング・パターンの平坦化を介して多重遷移単一モード同時発振が共通の上準位である（^{4}Ｆ$_{3/2}$**(1)**）からシュタルク分裂した異なる下準位である（^{4}Ｉ$_{11/2}$**(1,2,3)**）への遷移のもと発現する[5-6]。この際、**LFC** によるモード間の非線形相互作用が発現する。
この効果は、下準位原子の寿命と光子寿命の比に比例し

て増加し、ＬＮＰの場合、その比は６０程度となる。

その結果、多重モード発振に伴う低周波数側の緩和振動を基本とするパルセーションが限られた励起条件のもと発現する。図１に実験結果の一例を示す。反転分布グレーティングに基づく反位相ダイナミクスを反映して、モード出力の正弦的パルセーションは、総合出力において打ち消されている[7]。この反位相パルセーションは、ＬＦＣ効果を導入したレート方程式の解析とシュミレーションにより再現されている[8]。結果を図２に示す。

2．2　ＬＮＰ/ＫＴＰ 赤色レーザでのパルセーション

^{4}Ｆ$_{13/2}$を下準位とする１．３μｍの発振線を利用し、ＫＴＰをを用いた共振器内第二高調波発生においてＬＦＣを起源とする特異なパルセーションがが観測された。１mm厚のＫＴＰは遷移断面積が最大の^{4}Ｆ$_{13/2}$（１）への遷移波長１３１７ｎｍに対して位相整合させた。低励起レベルではこの遷移の安定な単一モードの２倍波が得られた。励起を上昇させると赤色への変換損失の少ない^{4}Ｆ$_{13/2}$（２）遷移１３３２ｎｍの２倍波での同時発振状態が達成さた。この際、２つの発振線は上準位を共有するΛ型遷移を構成している。なお、大きな位相不整合のため、両基本波の和周波は観測されなかった。

同時発振に伴い、図３に示すような特徴的な緩和振動パルセーションがそれぞれのモードについて観側された。対応するパワースペクトルも併記した。

図４には、波長変換およびＬＦＣ効果を導入したレート方程式定常解とその線形安定性解析から得られたスタビリティダイアグラムを、図５にはシュミレーション結果を示す。実験との極めて良好な一致が得られている。

スタビリティダイアグラムが示すように、下準位の寿命τＬが光子寿命τｐに比べて圧倒的に短い旧来の長共振器型固体レーザでは、量子干渉効果は顕在化し得ない。
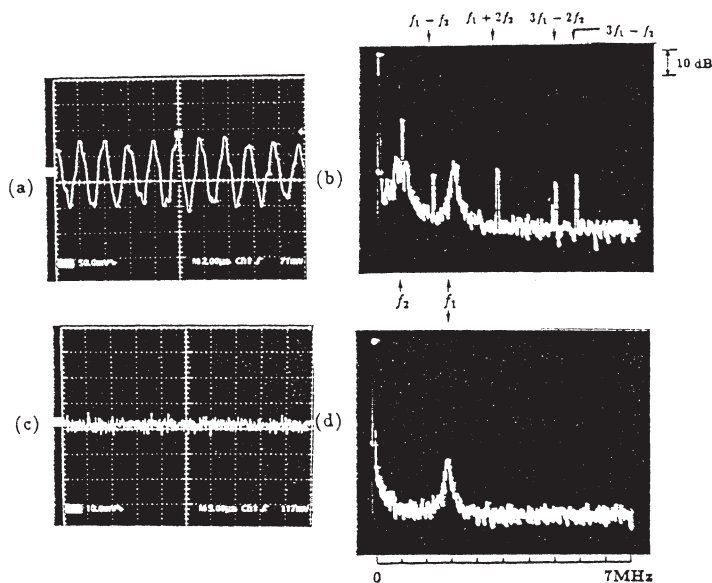
図1　１０５５ｎｍおよび１０６０ｎｍ多重遷移発振 LNP レーザでの反位相パルセーション（a），(b)：１０５０nm 出力波形と対応するパワースペクトル (c), (d)：総合出力波形とパワースペクトル。McCumber の緩和振動 f１以外はすべて反位相運動により総合出力で消滅している。モード出力には２つの緩和振動による混合成分が現れている。

図2　量子干渉を導入した２モード発振のシュミレーション結果（a）出力波形（ｂ）モード出力のパワースペクトル（ｃ）総合出力のパワースペクトル
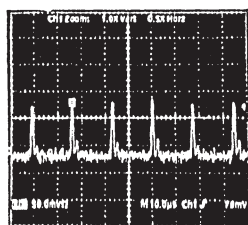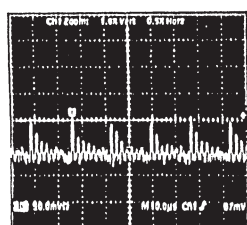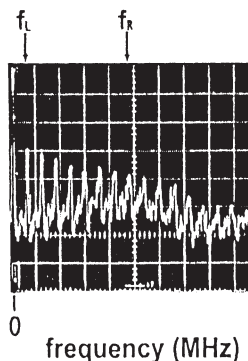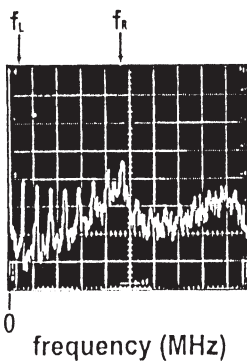
図3　多重遷移 SHG 赤色レーザ（LNP＋KTP）のパルセーション
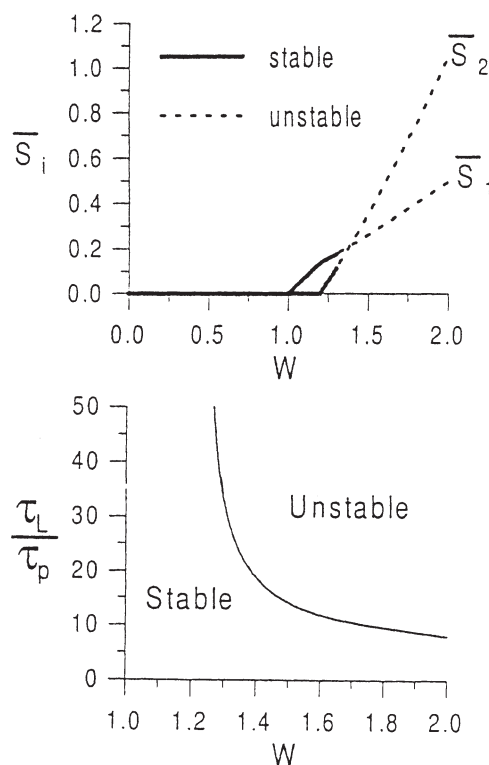
図4　量子干渉と波長変換を導入したレーザ方程式の定常解とその安定性（a）および下準位寿命対光子寿命比と相対励起に対するスタビリティダイアグラム。
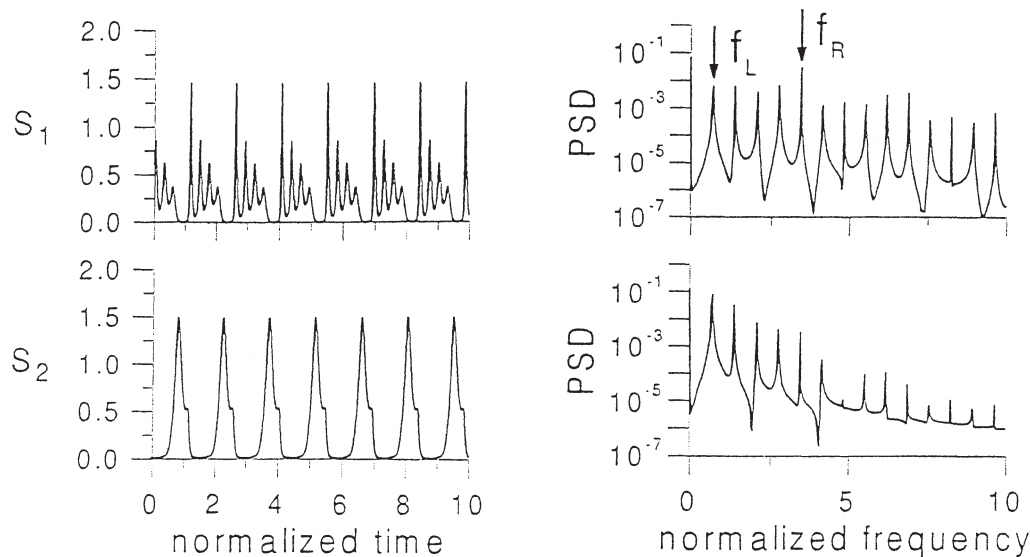
図5　多重遷移赤色レーザの量子干渉によるパルセー
ションのシュミレーション結果

3　1．5μmでのフォノン側帯波発光

　最近、我々は **Multi-wavelength Meter** を使用したL
D励起Ｎｄ系マイクロチップ固体レーザの発振スペク
トル測定に際して偶然に、１μm付近の基本発振線の
他に１．５μm付近の発光を見出した[9]。このような
遷移線はある筈がなく、様々な可能性を検討した。
Ｎｄ：ＹＡＧ、Ｎｄ：ＹＶＯ$_4$レーザでの１０６４．１
ｎｍの基本波長とのエネルギー差は、２９９７．１ｃ
ｍ$^{-1}$と極めて大きく、波長計への導入光ファイバでの
ラマン散乱は否定される。そこで、レーザ結晶自体で
のラマン散乱が疑われる。一般に、不準物原子の導入
によりフォノンエネルギーが活性化されることが知ら
れており、[10] 実際、ＮｄをドープしたＹＶＯ$_4$結晶で
は、２５００ｃｍ$^{-1}$程度に大きなフォノンエネルギー
が初期のラマン分光により報告されている[11]。ノンド
ープのＹＶＯ$_4$のラマン分光ではフォノンエネルギーは
最大のものでも１０００ｃｍ$^{-1}$程度である。我々は、
Ａｒレーザを励起光源としたラマン分光を行い、３０
００ｃｍ$^{-1}$付近にピークを観測した。　以上の考察よ
り、１．５μmの発光はフォノン側帯波の可能性が高
いと推察している。実験では、この発光には明確な励
起スレッショルドパワーが存在することが確かめられ
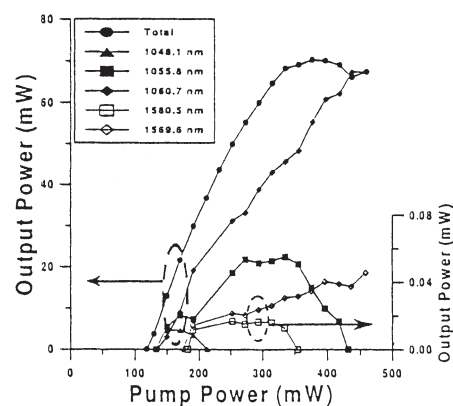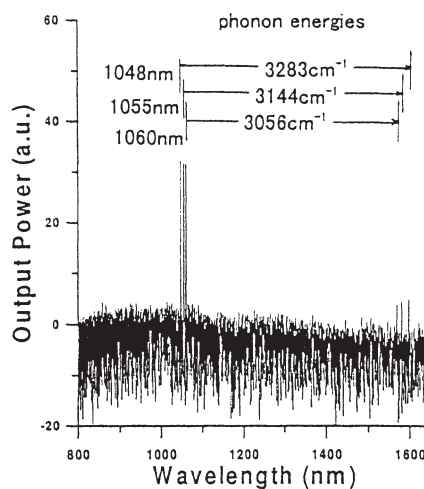
図6　多重遷移 **LNP** レーザの発振スペクトルおよび入
出力特性。

ており、共振器に閉じ込められ、極めて微少な励起領域での発振光電界とストークス光がフォノンを介して相互作用した結果、共振器内誘導ラマン発振が発現したものと解釈される。ストークス波に対する反射鏡透過率は５５％と大きく、最適なフィードバックとは考えられないが、基本波出力の約-３０ｄＢのパワー（５０μＷ）が得られている。

　同様の発振がＬＮＰにおいても観測されている[9]。しかしながら、Ｎｄ：ＹＡＧ、Ｎｄ：ＹＶＯ$_4$などの不純物添加型レーザとは異なる物性が出現する。２．１で述べた多重遷移発振に伴ない、エネルギーの異なるフォノンがそれぞれの遷移での発光に関与することが見出された。$^4I_{11/2}$（１，２，３）への遷移に対応した１０４８、１０５５、１０６０ｎｍでの同時発振

時における入出力特性および発光スペクトルを図６に示す。３つのエネルギーの異なるフォノンによる側帯波がそれぞれの遷移線に対応して発振していることが判る。

　以上述べた１．５μｍでのコヒーレントなレーザ光は、出力的には充分なものではないが、ＬＤを凌駕する優れた単色性を生かし、Ｎｄ系レーザの新たな可能性を期待させる。また、ＬＤ光により励起された電子が非放射遷移により準安定状態へ緩和する際に誘起される格子振動（フォノン）が内殻の電子遷移と相互作用し、如何なる散乱過程が発現しているのか、その物理的素過程の理解は興味深い光物性的な研究課題と思われる。

４　外部光帰還マイクロチップレーザ

　「ＬＤでの戻り光誘起不安定性」は、１９８０年の覧具・小林らによる先駆的研究に始まり、時間的に無限な自由度を持つ遅延帰還非線形系のプロトタイプとして、また、実用上の問題とも絡んで、膨大な研究が報告されている[12]。

　一方で、筆者は、１９７９年に、光ファイバーと結合した **Ar** レーザー励起マイクロチップ **LNP** レーザの多モード発振領域でランダムなカオス的バースト発生を観測していた[13]。この現象をマイクロチップ固体レーザを実用に供するための問題として再考するため、より安定な **LD** 励起での実験を再度用い、その物理的起源を追求した[14]。カオス的バーストの例を図７に示す。**LNP** の場合、この現象は極めて弱い光帰還時で、しかも多重の素子モード発振に限って生ずることが確認された。**Singular Value Decomposition** 解析および **Joint Time-Frequency Analysis** から、この現象は単一の外部共振器モードが、素子モードへの分配雑音に起因して安定状態と不安定状態間をランダムに遷移する非定常カオスであることが検証された。このダイナミクスは、マイクロチップレーザの外部戻り光に対する驚異的に敏感な応答に起因しており、**LD** での不安定性とは質的
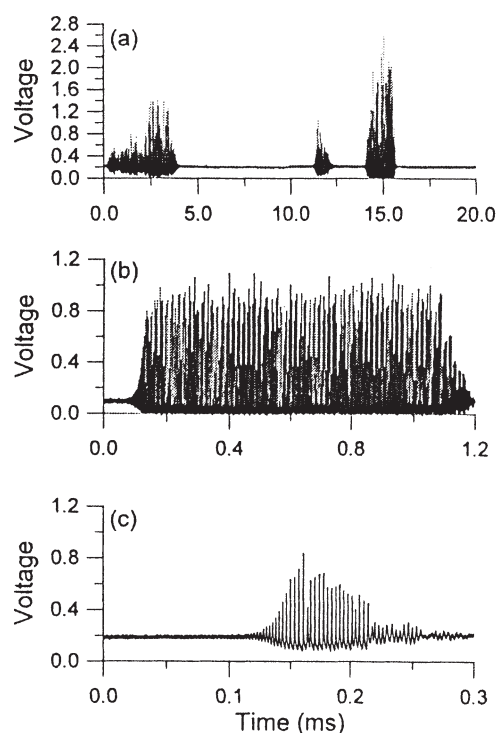
図７　**LD** 励起外部帰還２素子モード **LNP** レーザでのカオス的バースト。（１０ｍの単一モード光ファイバー端面からの反射による）

に異なる。

　戻り光量を増加させると、外部共振器モードは **LD** と同様に多モード化するが、**LD** での **Low Frequency Fluctuation (LFF)** は観測されず[15]、外部共振器モードの非線形相互作用の結果、外部共振器モード間隔周波数での正弦波的振動が発現する[14]。

　これらの現象は、レーザの量子ゆらぎ（**FM** 雑音）がカオスという決定論的不安定性を誘発して発現する。実際、**FM** ゆらぎ（線幅）が本質的に大きな（〜**MHz**）**Nd:YVO₄** レーザでの実験では、**LNP** と同様のバースティングが、単一素子モード発振時においても観測され、**FM** 雑音を印加した覧具—小林方程式の解析により検証された。観測波形とシュミレーション結果を図8に示す。なお、低雑音の **LNP** レーザ（線幅：数１００ｋ**Hz**）では、単一モード時には不安定バーストは生じない。また、外部共振器モードの正弦的振動もシュミレーションで再現されている。

　ここで述べた、戻り光誘起不安定発振は、次節で述べるように、マイクロチップ固体レーザでの極めて大きな蛍光対光子寿命比に比例して顕在化する発振光と戻り光との干渉効果とレーザに本質的に内在する量子雑音により発現しており、外部素子との接続など実用上注意を払わねばならない問題である。

5　**LD** 励起マイクロチップレーザの応用

5．1　超高感度速度・振動計測

　極めて大きな蛍光対光子寿命比 **K** に起因する戻り光に対する驚異的に敏感な応答を逆手に利用し、発振光と散乱戻り光の干渉に基づく自己光混合変調レーザドップラー振動計測システム（**LVS**）およびレーザドップラー速度計振動（**LDV**）を実現した。自己光混合による変調指数は電界の帰還率と **K** の積に比例し、０．３ｍｍ厚の **LNP** レーザでは $K=10^7$ に達し、ドップラービートサイクル当たり１フォトン以下の戻り光で動作する、運動方向弁別型 **LDV**[16-17]、およびｎｍの振
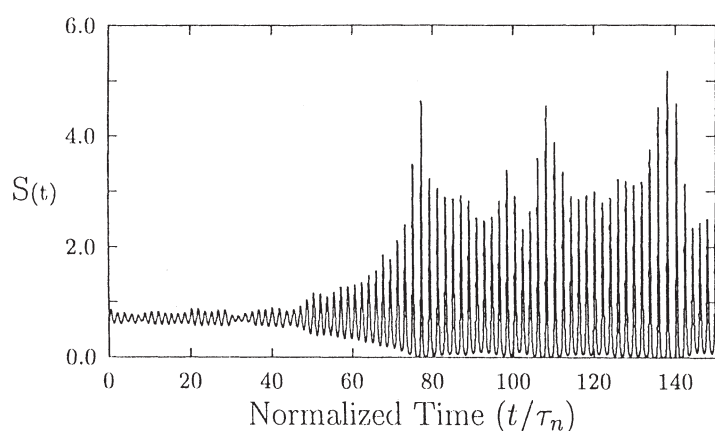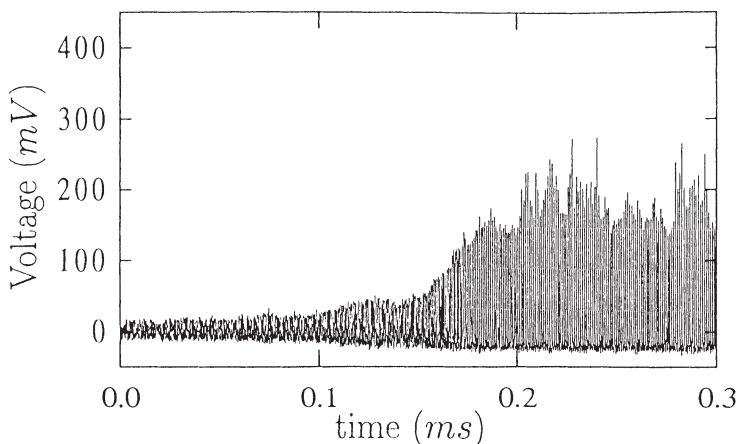
図８　**LD** 励起外部帰還単一素子モード **Nd:YVO₄** でのカオティックバースティングのたち上がり（ａ）実験結果（ｂ）量子雑音を導入したシュミレーション結果
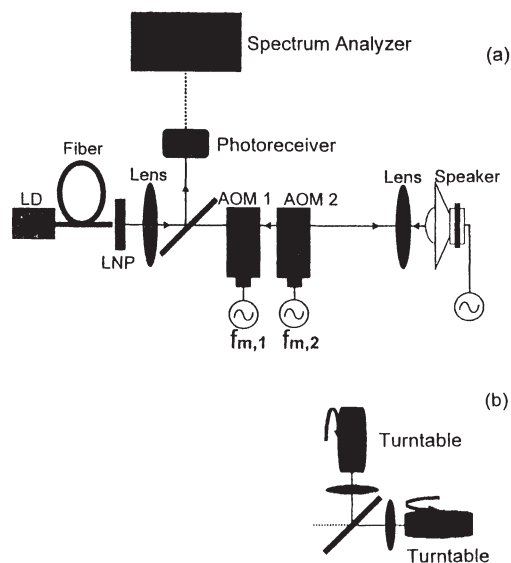
図９　自己光混合 **LVS** および **LDV** の測定系

動を計測できる **LVS** が実現されている**[18]**。図９に **LVS**、**LDV** の構成を示す。２台の音響光学変調器で光周波数シフトをかけ、ターゲットに入射させ、**LNP** レーザ出力のパワースペクトルをモニターした。

　図１０にスピーカー静止時および振動時のパワースペクトルを示す。**Al** の半球であるスピーカーの疎面での散乱帰還率は約０．３％と小さいにもかかわらず、約５０ｄＢのキャリア対雑音比が得られており、図１０(b)ではキャリアとＦＭ側帯波の強度比より振動振幅は約４．８ｎｍと求まる。振動振幅の測定限界は２ｎｍと見積もられる。また、これらの実験の過程でブリュリアン散乱などの超高感度分光や位相共役波発生への応用可能性を見出している**[17]**。

　図１１（ａ）には、運動方向弁別型の **LDV** の実験結果を示す。光ファイバーアクセスによる長距離リモートレンシング、立ち入り不能な装置内などの計測が可能である。図１１（ｂ）には、１０ｍの単一モード光ファイバでの計測結果を示す。また、ナノプローブや冷却原子群の運動のモニターへの応用も検討に値する。

10dB
スピーカー
静止時

10dB
スピーカー
振動時

4.9　　　　　　　　5.1
Frequency[MHz]
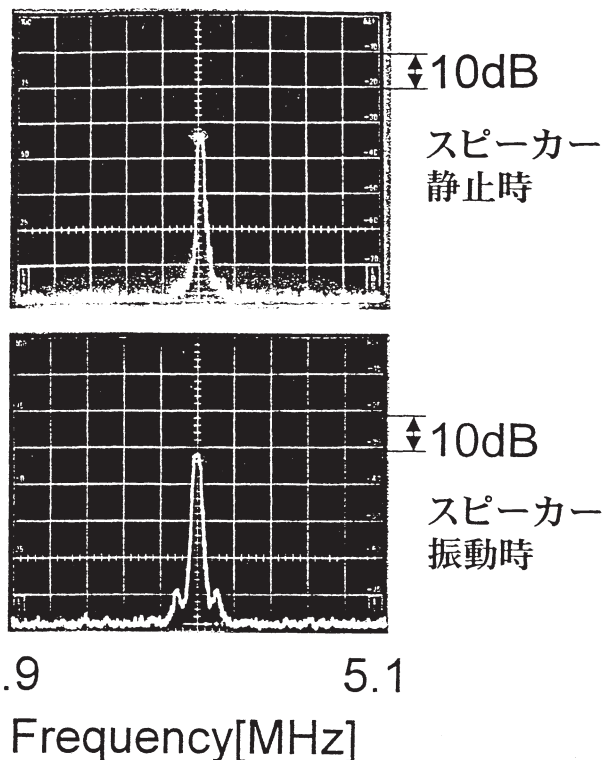
図１０　　**LVS** の実験結果　　(a)スピーカー静止（ｂ）振動時　　$2\Delta f_{AOM}=f_{m,1}-f_{m,2}=5MHz$

$2\Delta f_{AOM}$

10dB

(a)

-v ← | → +v

10dB

1　　　　　　3

Frequency, MHz
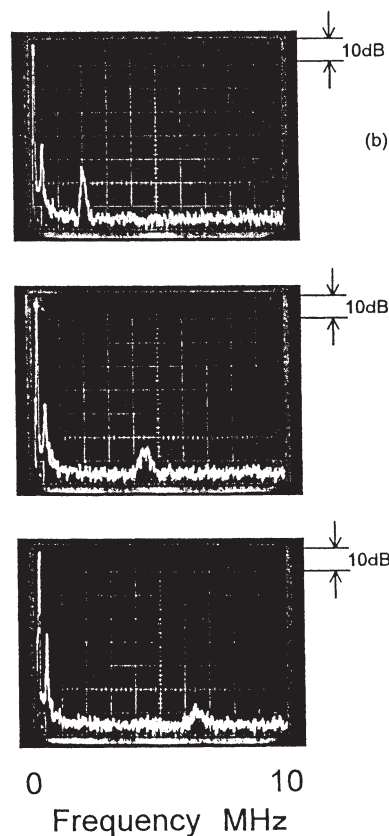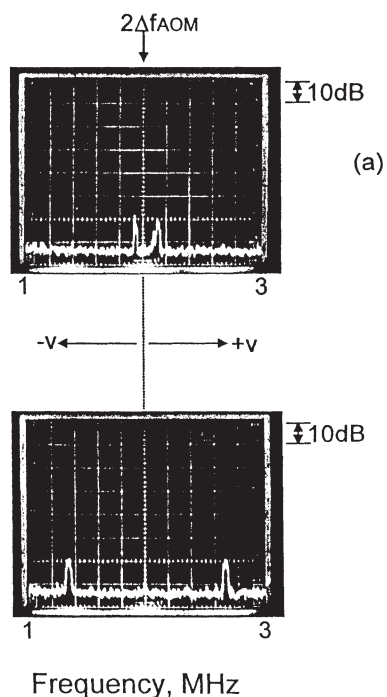
図１１　　**(a)**　　２つのターゲットを用いた方向弁別型 **LDV** の測定結果　　（ｂ）　１０ｍ単一モード光ファイバーでのセンシング（周波数シフター無し）

10dB

(b)

10dB

10dB

0　　　　　　　　10
Frequency　MHz

5．2　Green Laser without Green Problem

　ＫＴＰを非線形結晶としてＬＮＰレーザ共振器内に導入した第2高調波（SH）発生を行い、従来、実用上問題となっていた、和周波（SF）発生をもたらす隣接モード電場の混合に起因する動的不安定性（いわゆる、Green Problem）を回避したＳＨ、ＳＦ同時発振を実現した[19]。　図１２(a)の矢印のごく限られたポンプ領域においてのみ、モード出力（１０４８ｎｍの2倍波）は図１２(b)のように動的不安定性を呈するが、全出力では図１１(c)のように打ち消しあう、という反位相ダイナミクスが発現する。そのメカニズムはいまのところ理解できていないが、前述の１０４８、１０５５および１０６０ｎｍでの多重遷移単一モード同時発振によるLFCの形成が鍵を握っていることは間違いなさそうである。なお、この緑色レーザのスロープ効率は１０％であり、図１２（a）での●は、最大出力波長を示している。

　この安定な多重遷移緑色レーザは、大きな発振波長差を利用し、低温成長GaAsでの光混合による、THzコヒーレント電磁波発生への応用が期待できる。また、前節のLVS、LDVにも応用でき、緑色光をターゲッツへのRanging用に使い、微弱な漏れ基本波で自己光混合変調効果を発現させる方式で、容易なターゲットへのアクセスも確認している。

6　おわりに

　固体レーザに本来内在し、旧来の大型発振器では、陽に発現せず我々が見逃してきたと考えられる効果がマイクロ共振器構成にり顕在化し、量子干渉、誘導ラマン散乱に起因すると推察される現象を引き起こすことを述べた。また、マイクロ共振器構成による極めて大きな蛍光対光子寿命比に基づく、戻り光に対する驚異的に敏感な応答に直接起因して発現する、量子雑音誘起カオティックバースティングやこれを逆手に活用した自己光混合光計測への応用を紹介した。Green Problemを回避した多重遷移発振緑色レーザとそのTHzコヒーレント電磁波発生への応用可能性を論じた。
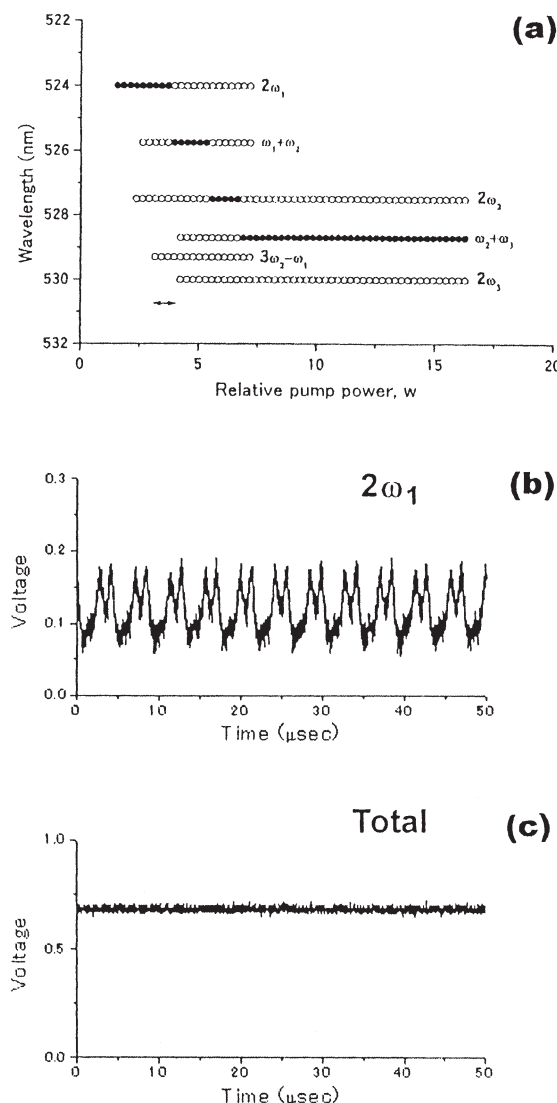
図１２　LNP＋KTP 多重遷移発振緑色レーザ

参考文献

[1] T. Yamada, K. Otsuka, and J. Nakano: J. Appl. Phys. Vol. 45 (1974) 5096.

[2] K. Kubodera and K. Otsuka: Appl. Opt. Vol. 18 (1979) 3882.

[3] K. Kubodera and J. Noda: Appl. Opt. Vol. 21 (1982) 3466.

[4] W. Koechner: *Solid-State Laser Enginnering* (Springer-Verlag, New York/Heidelberg/Berlin 1976)

[5] K. Otsuka, R. Kawai, Y. Asakawa, P. Mandel, and E. A. Viktorov: Opt. Lett. Vol. 23 (1998) 201.

[6] K. Otsuka, P. Mandel, and E. A. Viktorov: Phys. Rev. A Vol. 56 (1997) 3226.

[7] K. Otsuka, E. A. Viktorov, and P. Mandel: Europhys. Lett. Vol. 45 (1999) 37

[8] G. Kozyreff and P. Mandel, Phys. Rev. A 61 (2000) 033818

[9] S.-L. Hwong, J.-L. Chern, K. Otsuka, Y.-H. Huang, R. Kawai, and K. Ohki: Opt. Lett. Vol. 25 (2000) 646.

[10] B. Di Bartolo: *Optical Interactions in Solids* (Wiley, New York, 1968)

[11] J. R. O'Connor: Appl. Phys. Lett. Vol. 9 (1966) 407.

[12] R. Lang and K. Kobayashi: IEEE J. Quantum Electron. Vol. QE-16 (1980) 347.[13]

[13] K. Otsuka: IEEE J. Quantum Electron. Vo. QE-15 (1979) 655; K. Otsuka: *Nonlinear Dynamics in Optical Complex Systems* (Kluwer Scientific Publishers, Dordrecht/London/Boston, 2000) Chapter 4.

[13] K. Otsuka, J.-Y. Ko, J.-L. Chern, K. Ohki, and H. Utsu: Phys. Rev. A Vol. 60 (1999) R3389.

[14] I. Fisher et al.: Phys. Rev. Lett. Vol. 76 (1996) 220

[15] R. Kawai, Y. Asakawa, and K. Otsuka: IEEE Photon. Technol. Lett. Vol. 11 (1999) 706.

[16] K. Otsuka, R. Kawai, Y. Asakawa, and T. Fukazawa: Opt. Lett. Vol. 24 (1999) 1862.

[18] K. Otsuka, T. Fukazawa, N. Sekita, and S. Higashihara: Jpn. J. Appl. Phys. Vol. 39 (2000) L763.

[19] K. Otsuka, R. Kawai, and Y. Asakawa: Opt. Lett. Vol. 24 (1999) 1611.

RE³⁺ in Garnets: Relationship between Material and Laser Properties

Voicu LUPEI

Institute of Atomic Physics, National Institute for Lasers, Plasma and Radiation Physics
Quantum Electronics Laboratory, 76900 Bucharest, Romania

ABSTRACT

High resolution optical spectroscopy of trivalent rare earth ions in garnets put into evidence a large variety of spectral satellites induced by a discrete chain of mutual crystal field perturbations inside the ensemble of active ions in near crystallographic sites or of the ensembles formed by an active ion and defects or sensitizer ions. These satellites enable a selective investigation of the energy transfer processes inside these ensembles and verification of the energy transfer parameters determined from the global emission decay. The theory is illustrated for the case of Nd^{3+} in YAG. It is shown that an accurate description of the energy transfer processes leads to calculated quantum efficiencies that describe very well the observed concentration dependence of the quantum efficiency or of the fractional thermal load in this system. The importance of these processes for laser emission is discussed.

Keywords: laser crystals, garnets, energy transfer, quantum efficiency, solid-state lasers

1. INTRODUCTION

Owing to characteristics such as a very large variety of emission wavelengths or temporal regimes, to their high power and efficiency the solid state lasers constitute now the most popular class of lasers. To this contribute also their ruggedness, ease of operation and reliability. Despite of this the research in the field is very active, with the aim to extend the wavelength range, to identify tunable emission systems and to increase the total efficiency or the power of emission. This implies the identification of new laser transitions or new active media, the optimization of the systems already in use, new pump solutions and new resonator design.

A key in the identification of new transitions or laser media or for understanding the possibilities of improvement or the limits of the existing systems is an accurate and realistic modeling of the laser process that relates the laser characteristics for a specific temporal regime of emission with the properties of the laser material and with the conditions of pumping. This provides some lines of selection for the laser active media concerning both the transparent host medium and the ensemble of active ions as well as the combination of these two components. Additional criteria come from the necessity to assure a good heat dissipation and stable operating conditions as well as from technological or economic reasons.

Thus, the host medium should be fabricated economically in proper size with uniform and high optical quality (high transparency in the range of pump and emission wavelength ranges, low concentrations of scattering centers, no variation of the refractive index, no photochromic effects or color centers).

The host medium should have high hardness for good polishing and resistance to mechanical action, high stress fracture and optical damage thresholds, high thermal conductivity, small thermal expansion and small variation of the refractive index with temperature. It should incorporate uniformly the laser active ions in unique sites, preferably without the need for charge for

charge compensation. The sites should favor the conditions for an efficient population inversion: they should have low symmetry in order to favor the electric dipole transitions for pumping and emission and the electron-photon interaction should assure an efficient flow of excitation from the pump to the emitting level and from the terminal- to the ground level without strong effect on the lifetime of the emitting level.

The garnets, especially the trivalent structurally ordered $A_3B_2C_3O_{12}$ systems satisfy well these conditions. In these garnets all the three cationic species (A, B and C) are trivalent; despite the overall cubic symmetry of the garnet, all these cations are surrounded by O^{2-} polyhedra of lower symmetry: the large cations A occupy the dodecahedral-coordinated c-site orthorhombic D_2 symmetry, while the smaller ions B and C occupy the octahedral a-site (C_{3i} symmetry) and the tetrahedral a-site (S_4 symmetry), respectively; usually in these garnets the ions, B and C are identical. Typical such garnets are the yttrium aluminum garnet $Y_3Al_5O_{12}$ (YAG) and the gadolinium gallium garnet $Gd_3Ga_5O_{12}$ (GGG). These crystals are very good hosts for the trivalent laser active ions: the rare earth (RE) ions substitute predominantly the dodecahedral sites while the transition d-electron ions enter in the octahedral or/and the tetrahedral sites. The capability of the garnets to incorporate the doping ions depends on the ionic size mismatch but also on the method of fabrication: the crystals incorporate a much lower concentration of dopants than the thin films or the ceramic samples. A dependence of the composition on the temperature of fabrication is also observed: the high temperature systems, such as the melt grown crystals show departures the ideal stoichiometric composition an excess of 2 to 6 % of A ions, depending on composition of the garnet [1,2]; it was assumed that these excess A ions replace part of the B ions in octahedral sites. Such assumption was sustained by the X-ray investigation [3,4] that shows a disordering of the a-sublattice and by the EXAFS data [5] that show the presence in the melt-grown YAG crystals of three Y^{3+} - O^{2-} bonds, two of them

corresponding to the dodecahedral sites and one to Y^{3+} ions in octahedral sites. These effects are not observed in the low temperature (flux) – grown crystals. Moreover, EXAFS measurements suggested a large-scale (of about 10 %) of inversion between Y^{3+} and Al^{3+} (a) ions in YAG.

Another problem of concern is the possible existence of small amounts of anionic impurities such as OH^- revealed in some YAG samples. Such anions can induce localized vibrations larger than the lattice phonons: when localized in the neighborhood of the active ions, these anions can induce a very fast non-radiative relaxation of the excitation from levels above the metastable state, thus reducing the total emission efficiency without any effect on the emission decay of the metastable level. This model was invoked to explain the differences of the emission efficiency and the heating effects in case of Nd^{3+} - doped YAG and the Nd ions with a near OH^- impurity have been called "dead" Nd^{3+} sites [6, 7].

Despite of the expected simplicity in behavior, the high resolution spectroscopic investigation of the laser active ions in garnets as well as the measurements of some important parameters such as the quantum efficiency of emission of heating effects evidence in many cases concentration or fabrication method-dependent departures from the picture expected for isolated RE^{3+} centers occupying a unique structural site. This paper discusses such effects as the satellite structure of optical spectra, the concentration – and pump intensity-dependent departure from the exponential of the luminescence decay and their relation with the quantum efficiency and heating effects and finally with the laser emission properties. In order to illustrate more clearly this connection the paper will be concentrated on the most important laser active system, the Nd^{3+}- doped YAG, although reference to other active ions such as Tm^{3+}, Er^{3+}, Pr^{3+}, Yb^{3+} or to sensitized systems will be also made.

2. THE SATELLITES of the OPTICAL SPECTRA of ACTIVE IONS in GARNETS

As mentioned above, the garnets can be fabricated in different forms: bulk single crystals produced by high temperature melt – growth techniques (Czochralski, horizontal or vertical gradient methods) or by low temperature techniques (flux), thin films or ceramic samples. The ability to incorporate the dopant ions depends on the mismatch of their ionic radius with respect to that of the host cation and on the method of fabrication. Thus, in case of the melt grown YAG crystals the segregation coefficient is very low for dopant ions at the beginning of the lanthanide series (it equals 0.18 for Nd^{3+} in YAG) but it could be large (1 or even larger) for the ions at the end of the lanthanide series. Thus in case of Nd^{3+} doping, good quality YAG crystals can be grown from melt only up to about 1.5 at % Nd and the distribution of Nd^{3+} along the bole is non-uniform, lower at the beginning and larger at the end; however, in case of thin film samples the concentration of Nd^{3+} could reach 15at. % and for ceramic samples it could go up to over 9at. %. At the same time, good quality crystals can be obtained by doping with ions at the end of lanthanide series. At the same time the degree of non-stoichiometry depends on the temperature of fabrication: for YAG the percent of excess Y^{3+} ions in octahedral sites (Y^{3+}(a) antisites) is of about 1.75 – 2.5% in case of melt-grown (around 2000^{0}C) crystals but it is almost negligible for the flux grown (around 1400^{0}C samples; intermediate values

can be expected for the ceramic samples produced at temperatures of 1600^{0}C – 1700^{0}C.

Both the trivalent dopant ions and the antisites Y^{3+}(a) have the same electrical charge as the substituted host cations and thus there is not any reason for charge correlation in the occupation of the available YAG lattice sites. Thus the distribution of these centers in the crystalline lattice can be described by the statistics of the random equiprobable placement: if a given dopant ion is surrounded by a coordination sphere of m sites available to the dopant ions, the probability of having n of these sites occupied by other dopant ions is

$$P_{nm} = \frac{m!}{n!(m-n)!} C^n (1-C)^{m-n} \qquad (1)$$

where C is the relative concentration of the dopant.

Because of the differences between the ionic radii of the dopant ions or antisites and the host cations, they can induce local perturbations of the crystalline lattice that could sometimes extend over several coordination spheres. In the case of RE^{3+} ions substituting for Y^{3+} in YAG the mismatch runs from + 0.11Å or + 0.09 Å for Pr^{3+} and Nd^{3+} to –0.02 Å for Er^{3+} and- 0.03 Å for Tm^{3+} and Yb^{3+}; however, in case of the antisite Y^{3+} (a) the mismatch is much larger, of the order of 0.35Å, leading to a stronger lattice distortion.

When the dopant centers are well isolated from each other in the crystalline lattice, all these ions induce identical local distortions of the lattice and their optical spectra will be identical. However, when a dopant ion and a defect or another dopant ion are placed in near lattice sites additional mutual crystal field perturbations are produced, resulting in a shift of the energy levels and thus the optical spectra of these perturbed centers could differ from those of the isolated centers. These perturbations depend on the distance between the active ion and its associate and on the orientation of the perturbation with respect to the local symmetry axes of the center; because of this not all the positions on a given coordination sphere around the active ion are equivalent. Thus, owing to the discreteness of the crystalline lattice and to the various possibilities of placement of the perturbing center in the neighborhood of the active ion, a discrete chain of mutual crystal field perturbations can be obtained for each type of associations, leading to a specific multicenter (multisite) situation, manifested in the presence of typical structures of satellites in the optical spectra. The relative intensities of these satellites are proportional with the probabilities of occurrence of the perturbed centers given by eq. (1) provided that the equivalency of the perturbing effects produced from the various positions of a given coordination sphere is taken into account.

The most important types of associations that are possible in the garnet crystals are: (i) association of the active ions with antisite Y^{3+}(a) centers in near lattice sites (centers P_i); (ii) associations of active ions in near lattice sites: pairs (M_i), triads (T_i) and so on; (iii) association of the active ion with other doping ions such as the sensitisers in sensitized crystals, (iv) associations of the active ion with accidental anionic impurities such as OH^-; (v) association of the active ion with vacancies or color centers. However, not all these types have been observed by high resolution absorption at low temperatures: satellites P_i have been observed [4, 8-10] for practically all the dopant RE^{3+} ions in YAG (up to four resolved satellites of equal intensity, corresponding to the

perturbing effects of antisites from the first – and second coordination spheres) as well for Cr^{3+} substituted in octahedral sites [11]. The most encountered associations of active ions are the first-order M_1 (n.n.) pairs [4, 8-10], although in case of Nd^{3+} in YAG the pairs M_2 of second-order (n.n.n.) are also observed [4, 12]; in case of highly concentrated Nd samples satellites corresponding to triads of Nd ions in near lattice sites are also seen. Typical spectral satellites have been observed in the spectra of RE-doped garnets in case of sensitized crystals due to the perturbing effect of the sensitizer in octahedral – (Cr^{3+}) tetrahedral- (Fe^{3+}) or dodecahedral – (Yb^{3+}) sites [13]. Although several other much weaker satellites have been also seen, no structures clearly attributable to OH^- perturbations or to a large-scale a-c inversion of occupancy (as predicted by EXAFS) were identified. All the observed satellite structures could be explained only by assuming on overall cubic structure of the garnet lattice.   Thus the investigation of satellites is an important tool for investigation of details of the structure of the doped garnet crystals.

The satellites due to associations of the active ion with other active ions or with sensitizer ions could be very useful for a selective investigation of the energy transfer processes in laser crystals. With increasing temperature the resolution of the satellites is lost owing to the electron-phonon broadening of the lines. In samples of high activator concentration, where the ion pairs have a high concentration this leads to inhomogeneously broadened features suitable for diode pump.

The equivalency of the perturbations produced by the perturbing centers placed on the various sites of a coordination sphere can be established by calculating the crystal field perturbation or the line shift caused by each of these centers. Two methods can be used, the calculation of the strain-induced shift [14] or the calculation of the crystal field modification due to the anion displacements and to the charge redistribution induced by each perturbing center [15].

In several cases strong and sharp satellites that could not be attributed to perturbed centers have been observed in the vicinity of some spectral lines. Such satellites are in fact vibronic features whose intensity is enhanced due to the resonance of some crystal field splitting with the lattice phonons. Such effects have been observed for Yb or Tm in YAG [16, 17].

3. ENERGY TRANSFER in RE^{3+}– DOPED GARNETS

The energy transfer processes influence the flow of excitation in the active medium. Owing to the large variety of situations these processes could be either useful or deleterious. They can be static (direct) when the excitation of an ion (donor, D) excited from an external source or by transfer from another ion is transferred totally or partially to another ion (acceptor, A) or dynamic (migration assisted), when a migration on donors takes place prior to the transfer to acceptors.

The non-radiative energy transfer is a consequence of stationary (multipolar and/or exchange) interactions between donors and acceptors [18, 19]. The rates of transfer shows specific dependencies on the donor-acceptor distance for each of these interactions: for multipolar interactions $W_{DA}^{(s)} = C_{DA}^{(s)} / R_{DA}^s$, where s takes the values 6,8 or 10 for dipole-dipole (d-d), dipole-quadrupole (d-q) and quadrupole-quadrupole (q-q)

interactions, respectively and $C_{DA}^{(s)}$ is a specific microparameter that depends on the superposition integral of the donor emission and acceptor absorption. The multipolar interactions are governed by selection rules [20]: the quadrupole contributions are forbidden for transitions between levels for which $|J-J'|>2$. For the exchange interactions $W_{ex} = 1/\tau_D \cdot \exp\left[\gamma\left(1 - R_i / R_o\right)\right]$ where $\gamma=2R_oL^{-1}$, and L and R_o are the penetration depth and the effective Bohr radius; respectively.

The energy transfer processes can be investigated by their effect on the emission decay of the donor and/or the acceptor. In crystals each donor is surrounded by a specific configuration of acceptors and thus the global response of all the donors to the exciting pulse is $I = I_O \exp(-t / \tau) \exp\left[-P(t)\right]$, where $exp\ [-P(t)]$ is the survival probability in presence of transfer, averaged on all the possible acceptor configurations; function $P(t)$ is called transfer function. The process of averaging depends on the model used for the distribution of acceptors at the available lattice sites i. For a discrete random and equiprobable distribution of a unique type of acceptors of relative concentration C_A [21, 23]

$$P(t) = -\sum_{i=1}^{N} \ln\left\{1 - C_A + C_A \exp\left([-W_{DA}(R_i)]t\right\}\right. \qquad (2).$$

If the acceptors are placed on coordination spheres l, each containing m_l sites, 6, then

$$P(t) = -\sum_{l=1}^{N_l} m_l \ln\left[\left(1 - C_A\right) + C_A \exp\left(-W_l^{cr}t\right)\right] \qquad (3).$$

In case of a continuous and uniform distribution of the acceptors over the entire volume of the sample the transfer function can be written only for specific multipolar interactions [24]

$$P(t) = \frac{4}{3}\pi n_A \Gamma\left(1 - 3/s\right) C_{DA}^{3/s} t^{3/s} \qquad (4)$$

where $\Gamma(x)$ is the Euler function. At large times the transfer function for discrete acceptor distribution. Eq.(2) can be approximated by eq. (4) for continuous uniform distribution, usually with s=6. However, at short times the transfer function (2) can be approximated by a linear function of time.

The formalism of the transfer function enables an accurate rate equation description of the evolution of donor and acceptor populations

$$\frac{dn_D}{dt} = -\frac{n_D}{\tau_D} - \frac{dP(t)}{dt}n_D \qquad (5)$$

$$\qquad (6)$$

$$\frac{dn_A}{dt} = -\frac{n_A}{\tau_A} + \frac{dP_{DA}(t)}{dt}n_D - \frac{dP_{AA}(t)}{dt}n_A$$

where the transfer function $P_{AA}(t)$ accounts for the possible energy transfer processes inside the system of acceptor ions.

In presence of two types of acceptors that could occupy the same sublattice of the crystal the transfer function becomes

$$P(t) = -\sum_{i=1}^{N} \ln\left\{\begin{array}{l} 1 - (C_{A1} + C_{A2}) + C_{A1}\exp\left(-W_{DA1}(R_i)t\right) \\ + C_{A2}\exp\left(-W_{DA2}(R_i)t\right) \end{array}\right. \qquad (7).$$

For low acceptor concentration, function (7) can be written as a sum of two individual functions of type (2)

Institute for Molecular Science

corresponding to each of the two systems of acceptors.

The transfer functions of type (2) or (7) describe the global survival probability for the whole system of donors and their effect on the emission decay can be observed by detecting the emission of the whole system (the line corresponding to the isolated centers and the satellites corresponding to the various associations the donor ion with near acceptor ions). The observation of the spectral satellites shows that the system of donors and that of the acceptors cannot be considered as spectrally homogeneous but they can be viewed as consisting of homogeneous subsystems associated with the various spectral lines (the line of the isolated centers and the satellites corresponding to perturbed centers). The emission decay for each of these subsystems can be observed by selective excitation and detection. However, the effect of transfer on the decay in this case cannot be longer described with the transfer functions (2) or (7), obtained by averaging the survival probability of the donor over all the possible acceptor configurations and a new averaging procedures that take into account the peculiarities of the nearest neighborhood for each of these donor subsystems must be used [12, 13]. Thus in case of the perturbed donor centers there is always an acceptor ion in one of the near coordination spheres. If, for instance, the optical spectra reveal donor-acceptor pairs up to the second order (acceptor placed on the first or on the second coordination sphere around the donor), the transfer function for the perturbed centers will contain two parts: the transfer to the perturbing companion and the transfer to distant acceptors, outside, in this case, of the second sphere

$$P_i(t) = W_{DAi}(R_i)t + P_{DA}^{(d)}t \qquad (8)$$

where i indicates the order of resolved D-A pair and $P_{DA}^{(d)}(t)$ describes the distant transfer and has a form similar to eq. (2) with the summation truncated to exclude the sites from the spheres that give resolved perturbation. In turn, the transfer function for the isolated centers contains only the distant contribution.

This theory can be applied in case of the decay of emission from the metastable state $^4F_{3/2}$ of Nd^{3+} in YAG. The global emission decay at the room temperature of this level after a short (10nsec) nonselective low intensity excitation with the second harmonic (532 nm) of a YAG: Nd laser shows concentration-dependent departures from exponential. This effect can be attributed to a self-quenching energy transfer process inside the system of Nd^{3+} ions. Measurements function on Nd concentration show that up to about 1.5 at. % this transfer is static (direct) but above this concentration the presence of migration becomes obvious. This static transfer is down-conversion a cross-relaxation process between a Nd ion excited to the metastable state $^4F_{3/2}$ and another Nd ion in the ground state $^4I_{9/2}$. This down-conversion ($^4F_{3/2}$, $^4I_{9/2}$) → ($^4I_{15/2}$, $^4I_{15/2}$) populates the intermediate level $^4I_{15/2}$ from which the excitation relaxes to ground state all the excitation of the ion that acted as donor is transformed into heat [10].

The room temperature global emission decay of $^4F_{3/2}$, Nd^{3+} level in YAG is very unusual: the transfer function $P(t)$ defined as $- \left[\ln\left(I / I_0\right) + \left(t / \tau\right) \right]$ shows a very fast drop, of the extent of about $4C_{Nd}$ that ends practically within the first two microseconds of decay, followed up to about 30 μsec by a quasilinear dependence

of time, while at times larger than about 100μsec a $t^{1/2}$ dependence characteristic to a dipole-dipole interaction with the microparameter C_{DA} = 1.85 x 10^{-40} cm^{6}s^{-1} is observed. This interaction cannot explain the very fast drop at the beginning of decay but it accounts for almost the entire value of the slope W_{st} of the quasilinear portion of $P(t)$ provided the sum over the sites i excludes the firs coordination sphere around donor. The fast drop and the small misfit from W_{st} can be explained by the presence of an additional superexchange interaction (R_o = 5.43 Å , L = 0.54 Å) that dominates the energy transfer inside the first Nd ion pair, but it has a much less effect on the next pairs. These energy transfer parameters (C_{DA}, L, R_o) introduced in the transfer function (2) describe very well the observed decay under low pump, over the entire temporal range for samples with C_{Nd} up to 1.5 at.%. They are also verified by a consistent explanation with eq. (8) of the observed emission of the pairs M_1 and M_2 and of the isolated ions line N under selective excitation [12].

With increasing pump intensities the departures from exponential decay of $^4F_{3/2}$ Nd^{3+} in YAG is further increased, the effect being more evident at higher Nd^{3+} concentrations [25, 27] . This can be explained by the increasing effect of upconversion by energy transfer between two excited ions: by this process one of the ions is desexcited to one of the states $^4I_{15/2}$, $^4I_{13/2}$, $^4I_{11/2}$ or $^4I_{9/2}$ while the excitation of the other is raised to $^4G_{5/2}$, $^4G_{7/2}$, $^4G_{9/2}$ or $^2P_{1/2}$ respectively. The upconverted excitation returns almost completely to $^4F_{3/2}$ by multiphonon relaxation while the terminal level of the donor relaxes nonradiatively to the ground state. Thus by the combined effect of upconversion and of the fast multiphonon relaxation the donor is desexcited to the ground state and the acceptor returns in the excited state $^4F_{3/2}$; the physical effect is similar for all these four upconversion processes. This process prepares the donor from upconversion for the role of acceptor is down-conversion and the acceptor from upconversion for the role of donor of down-conversion or for a new role of acceptor in other upconversion act. Thus even at high initial population of the excited level the processes if down-conversion and of upconversion must be taken into account together [28] ; an excited donor can be considered as surrounded by two systems of acceptors, the Nd ions in ground state and the other excited Nd ions and, for C_{Nd} up to 1.5 at.% the transfer function $P(t)$ can be inferred from eq. (2)

$$P(t) = - \sum_{i=1}^{N} \ln \left\{ \begin{array}{l} 1 - C_{Nd} + rC_{Nd} \exp\left(-W_i^{up}(t)\right) \\ + [1 - r(t)]C_{Nd} \exp\left(-W_i^{cr}t\right) \end{array} \right\} \qquad (9)$$

where $r(t)$ is the fraction of Nd ions excited to the metastable level at any moment t and W_i^{up} and W_i^{cr} are the rates of transfer for upconversion and respectively for cross-relaxation for an acceptor placed at the site i. Owing to the temporal dependence

$$r(t) = r(0) \exp(-\frac{t}{\tau_D}) \exp\left[-P(t)\right] \qquad (10)$$

eq. (9) becomes transcendental and a simple analytical function for P(t) cannot be obtained: thus the theoretical description of decay needs a numerical solution. The analysis of eq. (9) coupled with eq. (10) shows that if strong short-range interactions hold inside the first (or several) order pairs, a fast drop should be again observed at the beginning of decay. If the rates of upconversion are lower than those of down conversion, the decay will be slower than for the low pump intensity, the effect being

more accentuated for high *r(0)* values. The opposite holds when the upconversion rates are larger than those for down conversion.

A comparison of the theoretical predictions with the experimental data on decay under high pump intensities is difficult since these data are collected apparently with low temporal resolution that does not evidence a fast drop at the beginning of decay. However, the analysis of the observed part of decay indicates that starting with the second coordination sphere the upconversion rates for Nd:YAG are very high, about 30-50 times larger than those for down-conversion measured at low pump intensity.

For Nd concentrations higher than about 1.5 at. % the migration on donors becomes evident in the low pump decay and this was accounted for by adding a concentration-dependent term $\overline{W} t$ in the equation (7) for the transfer function as suggested in [29]. This approach hides the detailed information on the ion-ion interaction; moreover, at high pump intensities the effect of migration immediately after the pump pulse is complicated by the low concentration of non-excited Nd ions.

This analysis of the decay could be extended for other RE^{3+} active ions or for sensitized systems. For instance, the analysis of the individual decays of the satellites induced by near sensitizer ions in the spectrum of active ion in case of Cr^{3+}of Fe^{3+} sensitized emission shows that a very selective mixed interaction behavior is manifested in the pairs of different order. Thus the presence of spectral satellites due the mutual crystal field perturbations inside the various ensembles of near active ions or active ions and sensitizers could be a very important means for a selective investigation of the energy transfer and for a better characterization of the global emission properties.

4. ENERGY TRANSFER EFFECTS on the EMISSION QUANTUM EFFICIENCY

The emission quantum efficiency η expresses the fraction of the ions from the metastable that desexcite nonradiatively. In presence of energy transfer the quantum efficiency is a product between the intrinsic quantum efficiency η_i determined by the balance between the radiative and nonradiative (multiphonon relaxation) desexcitation processes in the isolated ions, and the extrinsic efficiency η_v determined by the presence of energy transfer. Owing to the very high gap between the emitting level and the nearest lower level the intrinsic quantum efficiency of $^4F_{3/2}$ Nd^{3+} emission is very high even in the garnet crystals that have fairly high phonon energies: for Nd: YAG this intrinsic efficiency amounts to about 0.98.

The total emission efficiency of Nd: YAG was measured at low pump intensity by a variety of physical methods based either on the estimation of the effect of the loss mechanism on emission (modification of the decay lifetime at various Nd concentration with respect to the radiative lifetime or the reduction of the total emission intensity) or on the measurement of the heating of the sample or of the thermooptical or of the photoacoustic effects. Usually these data refer to Nd concentrations around 1at.% and they show an enormous spread from 0.47 to 1; in several cases different quantum efficiency values have been reported by measuring the same sample with different methods. In many cases the spread of

reported values is caused by the use of different values for some reference parameters such as the radiative lifetime or thermal parameters (thermal conductivity, the variation of the refractive index with temperature. However, in some cases physico-chemical of this variety g have been invoked, such as the presence of OH$^-$ anions in the vicinity of Nd^{3+} ions, that desexcite Nd^{3+} from levels above the metastable state $^4F_{3/2}$ (Nd "dead" sites). The absence of any satellite that could be clearly connected with the perturbing effect of OH$^-$ on the Nd^{3+} crystal field as well as the very low concentration of OH$^-$ groups evidenced by the infrared spectroscopy put this model under question.

Systematic measurements of quantum efficiency or of the heating effects in samples of various Nd^{3+} concentrations under low intensity pump show a very clear dependence of these parameters on C_{Nd}. Since the quantum efficiency in a decay experiment is defined by the area below the decay curve, these effects can be connected with the C_{Nd} dependence of decay in the presence of transfer. By using eq. (7) with the transfer parameters determined from decay the extrinsic quantum efficiency can be written as

$$\eta_t\left(C_{Nd}\right) = \exp\left(-bC_{Nd}\right) \tag{11}.$$

For C_{Nd} smaller than 1.5 at. % Nd the coefficient b is independent on C_{Nd} and can be calculated if the individual transfer rates are known

$$b = \sum_i \frac{W_i}{\tau_D^{-1} + W_i} = \sum_l m_l \frac{W_l}{\tau_D^{-1} + W_l} \tag{12}.$$

In case of Nd: YAG a lattice sum over 120 coordination spheres of dodecahedral sites around the donor gives $b \sim 20$. Thus for a Nd concentration of 1at.% the total quantum efficiency of $^4F_{3/2}$ emission under low intensity pump gives $\eta \sim 0.8$. This shows that the usual practice to assimilate the decay by an exponential and to neglected the initial drop, that gives for 1 at.% an efficiency of 0.9 is estimated by over 10 %. Eq. (11) imposes thus an upper limit for the quantum efficiency the global $^4F_{3/2}$ emission at low pump, owing to unavoidable nonradiative energy transfer losses.

Eq. (11) for quantum efficiency enables an analysis of the fractional thermal load defined as the fraction of the absorbed pump transformed into heat. Under monochromatic cw pump of low intensity in a level of energy Ep from which the excitation relaxes to the metastable level the fractional thermal load in absence of the laser emission is

$$\eta_h = 1 - \eta\frac{E}{E_p} = 1 - \eta_i \exp(-bC_{Nd})\frac{E}{E_p} \tag{13}$$

where E is the average photon energy quantum of the spontaneous radiative emission; in case of Nd: YAG it amounts to 9635cm^{-1}. Thus, for Nd^{3+} in YAG

$$\eta_h = 1 - 0.98\exp(-20C_{Nd})\frac{9635}{E_p} \tag{14}.$$

The data measured under 808nm pump in Nd: YAG are very well described by eq. (14) without the need to resort to the assumption of the existence of dead sites.

At high pump intensities the on-set of upconversion could modify the quantum efficiency. For upconversion rates smaller than those for down conversion the emission quantum efficiency is larger than that predicted by eq. (11) the effect being more

pronounced at high $r(o)$ values while for larger rates of upconversion the situation is reversed. This analysis shows that the quantum efficiency [30] and the heating effects [31] in Nd: YAG can be well described by taking into account an accurate picture of the energy transfer processes. These processes impose an upper limit on efficiency and only when the measurements show undoubtedly lower values, other causes must be identified.

In presence of laser emission the transfer processes influence only the spontaneous emission from the population of the emitting level clamped at the threshold value for inversion. In case of a high laser extraction efficiency (low threshold) the heating effects in laser emission regime are determined essentially by the quantum defects. In case of Nd: YAG this recommends the pump in the emitting level, preferably in the room temperature broad feature corresponding to the transitions from the second and third stark level of the ground level to the lines R_1 and respectively R_2 of the emitting level ${}^4F_{3/2}$: this pump is very suitable for highly concentrated samples where the satellites corresponding to Nd^{3+} pairs broaden the absorption band assuring condition for a stable diode pump.

5. CONCLUSIONS

The high resolution optical absorption and emission spectra and emission decay of RE^{3+} ions in structurally-ordered garnets such as YAG or GGG show a very complex behavior, manifested by the apparition of spectral satellites and by a complex concentration and pump intensity – dependent temporal evolution of the global or selectively excited emission caused by the energy transfer.

The spectral satellites are caused by the resolvable mutual crystal field perturbations inside the various associations of the active ions or of such ions and other dopant ions (such as the sensitizers) or defects. The structure and the relative intensities of these satellites depend both on the concentration of the dopant ions and of defects and on the crystallographic structure of the host crystal. The presence of these satellites gives ground to consider the system of active ions as spectrally inhomogeneous, but composed of homogeneous subsystems corresponding to various associations of ions or ions and defects. These subsystems are further individualised by a selective manifestation of the energy transfer processes.

The emission decay of several RE^{3+} ions in YAG evidences complex energy transfer governed by multiple interactions containing multipolar electric interactions and a short-range superexchange interaction acting in the near-ion pairs. In case of Nd^{3+} in YAG, at low pump intensities, the ${}^4F_{3/2}$ emission is influenced by a down-conversion cross-relaxation on intermediate levels caused by superexchange and dipole-dipole interactions; the absence of quadrupolar contributions is in agreement with the selection rules for the transitions involved in transfer. The energy transfer parameters determined from the global decay are verified from the emission of the selectively excited pairs of the first and second-order and of the line of the isolated ions. The pairs formed by activators and sensitizers are important in the investigation of the sensitization process.

At high pump intensities the problem can be complicated by the onset of upconversion processes from the metastable state. In case of Nd: YAG an unitary treatment that takes into account the simultaneous presence of upconversion and down-conversion is necessary in order to give an accurate description of emission under high pump.

An accurate description of the effect of the energy transfer on the emission decay enables a direct connection of the quantum efficiency of emission with the parameters describing the energy transfer and the spectroscopic properties of the active system. Thus a unitary treatment of the satellite structure of the spectra, of emission decay in various conditions and of the quantum efficiency can indicate new lines of action for improving the performances of the solid state lasers.

REFERENCES

[1] V. Lupei, A. Lupei, Phys. Rev.B, 61,8087 (2000).
[2] S. Geller, G. P. Espinosa, L. D. Fullman , P.B. Crandall, Mater. Res. Bull. 7, 1219 (1972).
[3] J. Cchenevas, J. C. Joubert, M. Marezio, B. Fernarnd, J. Less Common Met. 62, 373 (1978).
[4] V. Lupei, A. Lupei, C. Tiseanu, S. Georgescu, C. Stoicescu and P. M. Nanau, Phys. Rev. B 95, 8 (1995).
[5] Jung Dong , Kunquan Lu, Phys. Rev. B43, 8808 (1991).
[6] D. P. Devor and L. G. DeShazer, Opt. Commun. 46, 97 (1983).
[7] D. P. Devor, L. G. DeShazer and R. C. Pastor, IEEE J. Quantum Electron. 25, 1863 (1989).
[8] V. V. Osiko, Yu. K. Voronko and A. A. Sobol, in Crystals 10 Springer-Verlag, Heidelberg, Berlin (1984) p. 87.
[9] V. Lupei, A. Lupei, S. Georgescu and C. Ionescu, Opt. Commun. 60, 59 (1986).
[10] A. Lupei, V. Lupei, S. Georgescu and W. M. Yen, J. Luminesc. 39, 35 (1987).
[11] V. Lupei, L. Lou, G. Boulon, A. Lupei, J. Phys.: Condens. Mat. 5, 135 (1993).
[12] A. Lupei, C. Tiseanu, V. Lupei, Rad. Effects and Defects in Solids, 136, 23 (1995).
[13] V. Lupei, A. Lupei and G. Boulon, Phys. Rev. B 53, 1 (1996).
[14] A. M. Stoneham , Rev. of Modern Phys. 41, 82 (1969).
[15] D. J. Newman and B. Ng, Rep. Progr. Phys. 52, 699 (1989).
[16] A. Lupei, V. Lupei, J. Phys. Condens. Mat. 9, 2807 (1997).
[17] A. Lupei, V. Lupei, V. N. Enaki, C. Presura, A. Petraru, Spectrochim. Acta A55, 773 (1999).
[18] T. Forster, Ann. Phys. 2, 55 (1948).
[19] D. L. Dexter, J. Chem. Phys. 21, 836 (1953).
[20] T. Kushida, J. Phys. Soc. Japan 34, 1319 (1977).
[21] S. I. Golubov and Yu. V. Konobeev, Sov. Phys. Solid State 13, 2679 (1972).
[22] V. P. Sakun, Sov. Phys. Solid State 14, 1906 (1973).
[23] A. Blumen and J. Manz, J. Chem. Phys. 71, 4694 (1979).
[24] M. Inokuti and F. Hirayama, J. Chem. Phys. 43, 1078 (1965).
[25] Y. Guyot, H. Manaa, J. Y. Rivoire, R. Moncorge, N. Garniers, E. Descroix, M. Bon and P. Laporte, Phys. Rev. B 51, 784 (1995).
[26] S. Guy, C. L. Bonner, D. P. Shepherd, D. C. Hanna, A. C. Tropper and B. Ferrand, IEEE J. Quantum Electron. 34, 900 (1998).
[27] M. Pollnau, P.J.Hardman, M.A. Kern, W. A. Clarkson and D.C. Hanna Phys. Rev. B. 58, 16076 (1998).
[28] V. Lupei, Opt. Mater. (in press).
[29] I. A. Burnshtein, Sov. Phys. Uspekhi, 27, 579 (1984).
[30] K. K. Deb, R. G. Buser and J. Paul , Appl. Opt. 20, 1203 (1981).
[31] T. Y. Fan, IEEE J. Quantum Electron. 29, 1457 (1993).

原稿受付日	平成 12 年 9 月 28 日

材料加工用サブピコ秒 Yb:YAG レーザーの開発

藤田雅之、井上典洋、山中千代衛　　佐野英作、久保亮一、井澤靖和
（レーザー技術総合研究所）　　（大阪大学レーザー核融合研究センター）

Development of Sub-ps Yb:YAG Laser for Material Processing

Masayuki Fujita, Chiyoe Yamanaka (Institute for Laser Technology)
Eisaku Sano, Ryouichi Kubo, Yasukazu Izawa (Institute of Laser Engineering, Osaka Univ.)

Abstract

The use of sub-ps laser pulses for material processing results in very precise cutting and drilling with high efficiency, although the energy of such a ultra-short laser pulse is essentially small.　In order to accomplish high throughput for the industrial applications, it is required to operate the laser system at a high average power and thus at a high repetition rate.　Yb:YAG has a high potential to fulfill such requirements.　In this report, we summarize our current status of the developments of a LD-pumped femtosecond Yb:YAG MOPA laser system.　Performances of the Yb:YAG oscillator and the broadband gain characteristics ($\Delta \lambda \sim 71$ nm) are described.

キーワード：フェムト秒レーザー、Yb:YAG、レーザー加工、半導体レーザー励起
(femtosecond lasers, Yb:YAG, laser material processing, laser-diode pumping)

１．はじめに

　近年の超短パルスレーザー技術の目覚ましい発展に伴い、様々な応用分野での超短パルスレーザー利用が進展している。特に、超短パルスを用いたレーザー加工は、熱が周囲に伝わるよりも短い時間でレーザーが照射されるため、1）周囲に熱変成のない加工が可能、2）熱損失が少なく、エネルギー利用効率が高い、3）加工の制御性が良い、などの特徴を有しているため産業界の注目を集めている。一方、超短パルスレーザーはパルス当たりのエネルギーが小さいため、産業用の高処理能力を達成するためには、パルスの高繰り返し化が必要となる。しかし、現状の超短パルスレーザー装置のパルス繰り返し率は 10Hz ないし 1kHz にとどまっており、研究用のツールとして利用されているにすぎない。
　超短パルスレーザーに限らず、これまでのレーザー開発はレーザー媒質の性質に基づいて装置の仕様が決められてきた。従って、与えられたレーザー装置の仕様にたまたま合致した用途でのみレーザー応用が進展してきたと言える。超短パルスレーザー加工のように利用価値の高い物理現象を実用化へ結びつけるためには、これまでとは異なるレーザー開発の姿勢が必要であると考えられる。即ち、応用の要求に応じてレーザー装置の仕様を決め、個々の応用に最適化された装置を開発することが重要となる。

　以上のような背景から、我々は超短パルスレーザー加工の有用性に着目し、産業用を目指した加工に最適化された超短パルスレーザー装置の開発を進めている。

２．加工用超短パルスレーザーの仕様

　超短パルスレーザー加工に最適化されたレーザーシス
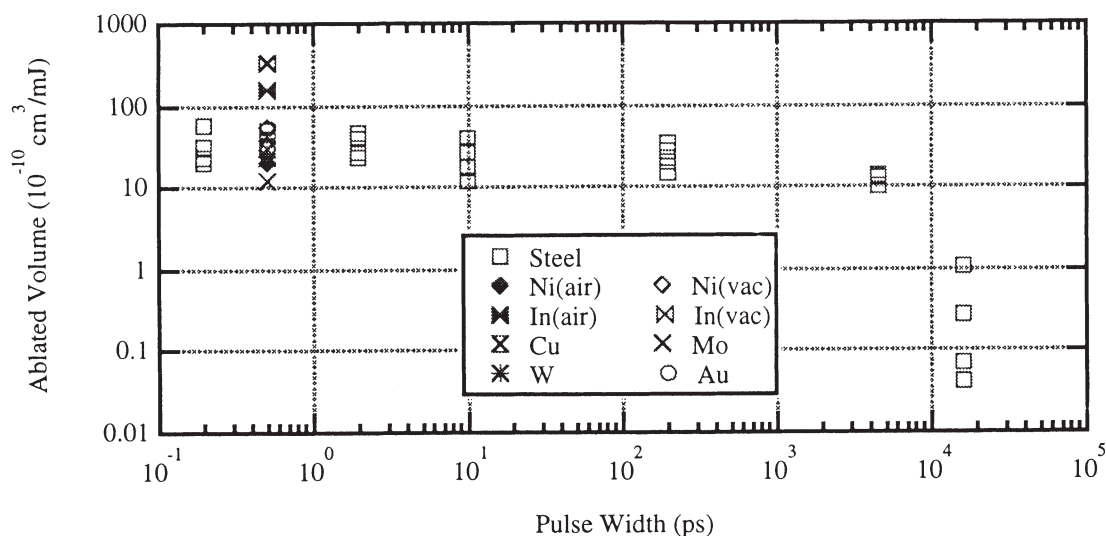
Fig.1　Ablated volume as a function of laser pulse width [1-5].

テムの仕様を以下のように検討した。

1）パルス幅：100〜500 fs（＜1 ps）

　シングルショットでの超短パルス加工はこれまでに研究がすすめられ、パルス幅とパルス当たりの除去体積の関係がすでに調べられている [1-5]。Figure 1 に文献より得られた金属加工データのまとめを示す。エネルギー当たりの除去体積は、パルス幅数 10ns の場合に比べて ps 以下の場合は 10 倍近く改善されることが分かる。100fs 以下のパルス幅ではさらに改善されるが、パルス幅が短くなるとパルス当たりのレーザーエネルギーが小さくなり、さらにはレーザーシステムも複雑になる。そこでパルス幅として高効率・高精度な材料加工を行うために、100〜500 fs のサブピコ秒パルスレーザーが最適であると考えられる。

2）パルス繰り返し率：0.1〜1 MHz

　フェムト秒レーザーはパルスエネルギーが小さいため、加工の高処理能力を達成するためには、なるべく高い繰り返しでパルスを発生させ、高い平均パワーでレーザーシステムを動作させる必要がある。

　一方、超短パルスレーザー加工の有用性を維持するためにはプラズマとの相互作用を避ける必要性がある。即ち、レーザーエネルギーがプラズマに直接吸収されると、不要な熱エネルギーとして消費されるため、レーザーパルスは常に固体表面を照射する必要がある。

　従って、繰り返し率はプラズマの持続時間よりも長い

間隔でパルスを発生させるという制限を受ける。プラズマダイナミクスよりプラズマの持続時間 τ_p は L/c_s で評価することが出来る。L はプラズマのスケール長またはレーザーのスポットサイズであり c_s は音速である。$c_s \sim 10^6$ cm/s、L〜1mm の典型的な値について、τ_p は 10^7s の程度となる。これは 10MHz の繰り返しに相当するが、実際にはその1/10の 1MHz の繰り返し率が最大と考えられる。また、機械的な反応速度（加工対象物の移動速度などレーザーやプラズマ以外の要因）から実用的な値として 0.1MHz に制限されることも考えられる。

3）　パルスエネルギー：10〜100 μJ

　一般的な金属のアブレーション閾値は 1〜0.5 J/cm^2 であることから、効率の良いアブレーションを行うためには閾値の 2、3 倍を達成する必要がある。30μm〜100μm のスポット径に対して、パルスエネルギーはそれぞれ 10μJ〜100μJ に相当する。

　以上の 1）〜3）より、本研究で目標とするレーザーシステムは、パルスエネルギーとして 100μJ を用いると、最大でピークパワーと平均パワーはそれぞれ 100μJ / 500 fs = 200 MW と 100μJ×1 MHz=100 W に相当する。

3．超短パルスレーザーとしての Yb:YAG

　最近、半導体レーザー励起の全固体化レーザーを念頭にした近赤外領域に吸収域をもつ結晶について短パルス

発生の研究が活発に進められいる[6]。半導体レーザーの品質向上により、半導体レーザーや半導体レーザー励起固体レーザーが励起光源として利用可能となり、小型化が進んでいる。特に、半導体レーザー直接励起可能な超短パルス用新固体レーザー媒質として Yb ドープレーザーは注目を集めている。

　Yb ドープ媒質は吸収波長が 900 nm 帯にあることから Al フリーで長寿命の InGaAs 系高出力半導体レーザーを励起光源に使うことができる。また、Yb イオンの優位な点は、レーザー遷移に伴う量子欠損が小さく、その単純な電子構造は ESA（excited-state absorpption）、アップコンバージョン、クエンチングのようなロスを避けることができる。Yb ドープ媒質の効率の良さは、すでに Yb:YAG などの CW 状態において実証されている。そして、Yb イオンの長い蛍光寿命（1〜2 ms）はとりわけ高出力超短パルス増幅のために有利である。また Nd と比較して広い吸収、蛍光スペクトルを持つ点も優位である。特に、ホスト結晶として熱伝導の良い YAG を用いることで高平均出力時の熱負荷を緩和させることが期待できる。

　一方、Yb ドープ媒質を用いる上で最も厳しい点は、エネルギー準位が準 3 準位レベルであることから、発振には吸収飽和を必要とすることである。これまで Yb の高効率という長所を発揮するには Ti:sapphire laser、LD 励起固体レーザーのような回折限界近くの励起源を供給しなければならなかった。しかしながら、最近の半導体レーザーのビーム品質の急速な向上により、Yb ドープ媒質に要求される飽和強度以上の高い励起強度が達成できるようになってきている。

4．LD 励起 Yb:YAG レーザー発振器の試作

　LD 励起高繰り返し超短パルスレーザー材料の候補として Yb:YAG 結晶の特徴に着目し、産業応用に向けた高繰り返し短パルスレーザーシステムの開発を進めている。第一段階として、LD 励起 Yb:YAG レーザー発振器を試作し、その基礎特性の測定を行った。

　発振器の光学配置図を Fig.2 に示す。共振器は超短パルス発生用 X 型共振器構造をとっている。M1〜M4 が共振器ミラーで、M1 の出力鏡としてはλ=1030 nm で 94.4 ％と 99.9 ％の反射を持つものを用いた。M4 の反射鏡は 1030 nm で HR コート 100 ％のフラットミラーである。M2 及び M3 は曲率半径 100 mm のもので、励起波長 940 nm では M2 で約 95 ％、M3 で約 70 ％の透過率を持つ。各ミラーは Yb:YAG の発振波長λ=1020〜1060 nm を十分カバーする 1000〜1120 nm に高反射コーティングされている。LD 光は 4 枚のレンズを用いて水平方向のみシリンドリカルレンズで 10 倍になる拡大光学系を組み、結晶上に集光した。集光ビームサイズはナイフエッジ法を用いて測定した。半値全幅（FWHM）で水平方向では 160 μm、垂直方向では 27 μm に集光できていることがわかった。励起光には 1.6W の半導体レーザーを用いたが、集光光学系での損失により結晶端面に入射する実際のパワーは 1.26W であった。従って入射光最大強度は、37kW/cm^2 と計算される。Yb:YAG の吸収飽和強度（hν/$\sigma\tau$）は 26.47kW/cm^2 であるため、充分な励起強度が得られたこととなる。

　Yb:YAG 結晶は、Scientific Materials 社製のドープ濃度 5 at.%、厚み 5 mm のノーコートのものを用いた。結晶は共振器中にブリュースター配置したため、媒質長は 3.4 mm になる。結晶は銅製のヒートシンクにインジウムホ
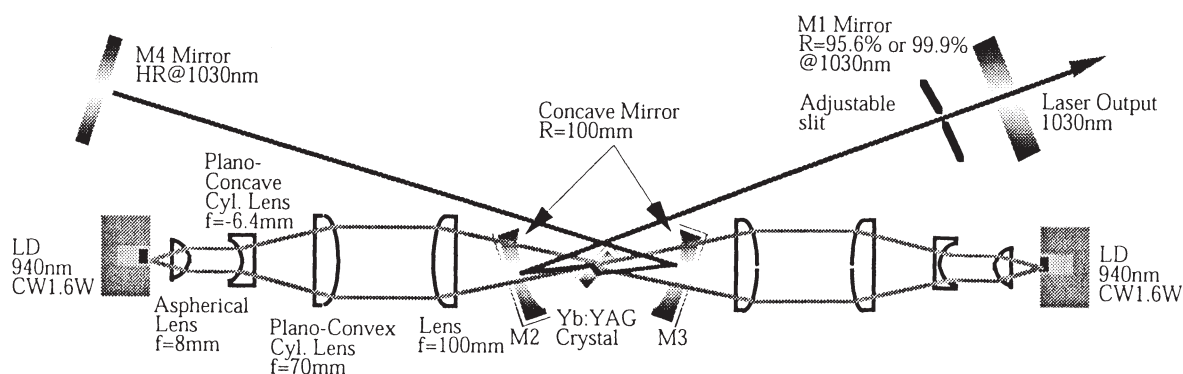

Fig.2　Layout of the Yb:YAG oscillator.

イルを介して固定した。

　フリーランニングにおいては、励起パワーに対する出力パワーは片側励起でスロープ効率 9.6 %、発振閾値 748 mW、最大出力 52 mW であり、両側励起ではスロープ効率 12.1 %、発振閾値 1078 mW、最大出力 143 mW であった。発振の中心は 1029.9 nm で確認することができた。

　また、複屈折フィルターを共振器中に挿入すると、挿入していないときの出力と比較して最大で約 3 倍の出力が得られた。その結果を Fig.3 に示す。励起パワーに対する出力パワーは片側励起ではスロープ効率 35 %、レーザースレッシュホールド 540 mW、最大出力 240 mW であり、両側励起ではスロープ効率 36.5 %、レーザースレッシュホールド 832mW、最大出力 498 mW であった。このときの発振波長は 1048 nm 付近であった。このような結果が得られた原因としては複屈折フィルターによる偏光の補償や共振器モードサイズの変化による励起光とのマッチング効率が上がったためであると考えられる。

　Yb:YAG レーザーの繰り返し発振の特性を調べるため
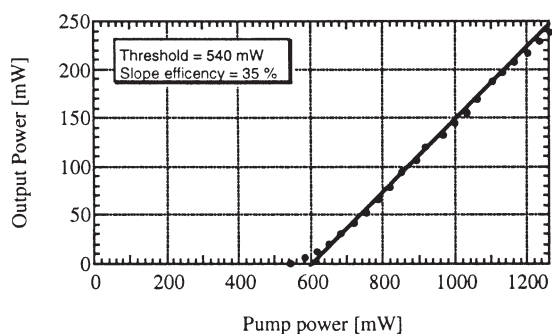
(a) Single side pumping
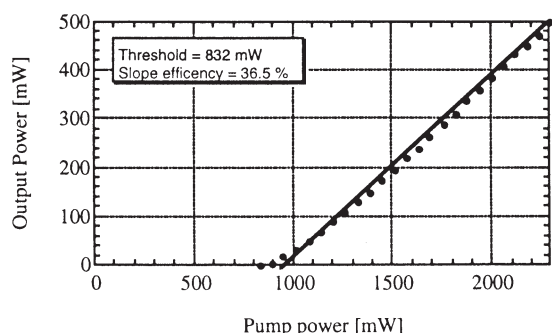
(b) Double side pumping

Fig.3　Yb:YAG output as a function of pump power with birefringent filter.

に、Fig.2 の共振器中にオプティカルシャッターを設置し、Q スイッチ動作によるパルス発振特性の測定を行った。このチョッパーはスリットが等間隔に開いている 4 種類の円盤を（一つの円盤にスリットが 2、5、10、30 個等間隔に開いている）モーターに取り付けて、最大回転数 100 Hz で回転させた。結果を Fig.4 に示す。この測定結果から、CW 励起で高繰り返し動作を行ってもエネルギーを抽出できることがわかった。

　Yb:YAG の利得幅は、1026〜1035 nm と広く、エネルギー構造がシンプルであるため利得幅を超えた波長領域での発振も可能であり、短パルス発生にも適した材料である。そこで、今回試作した Yb:YAG 発振器において実際どれだけの短パルス光発生の可能性を持っているかを調べるため、Yb:YAG の波長可変域測定を行った。測定方法は Fig.2 に示す共振器内部へ複屈折フィルター（厚さ 1 mm の水晶）をブリュースター配置で挿入し、一方向に 0.33 °づつ角度回転させた時に発振しているレーザー光を分光器へ通し、波長を測定した。そして各波長ごとの出力もパワーメーターで測定した。

　We measured the tunability performance of the Yb:YAG to investigate the possibility of ultrashort pulse generation and amplification. To evaluate the tunability, we introduced a birefringent filter into the cavity. Figure 5 shows tuning curves of the Yb:YAG laser using a 1-mm-thick quartz birefringent filter. The solid circles are tuning range which was measured with the output coupler reflectivity of 94 %. The solid triangles were measured with the output coupler
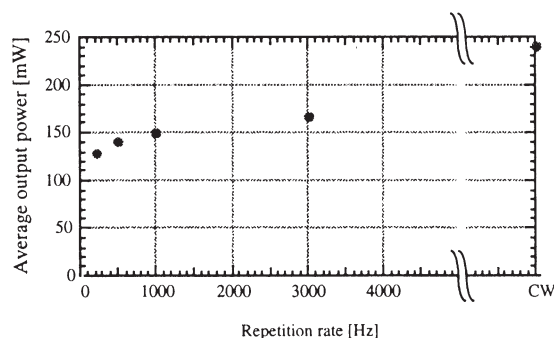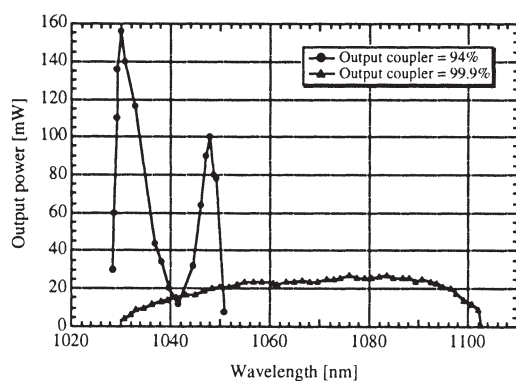

Fig.4　Q-switch output at various repetition rate.

reflectivity of > 99 %. Although the solid circles correspond to the tuning range which is reported in another literature[7], the solid triangles shows broader tuning range from 1031 to 1102 nm. The only difference was the output coupling. This wide tunable (71 nm, 18.7 THz) range corresponds to Fourier-transform limit pulse of 17 fs.

The observed broad tuning range can be explained by the spectrum properties of the Yb:YAG crystal. The absorption and the emission cross section of the Yb:YAG crystal used in the experiments are shown in Fig.6 (a). The Yb:YAG crystal has several peaks in the emission cross section. Although 1030nm line is the generally observed oscillation wavelength, it overlaps with the absorption peak. The 1050nm line is another oscillation wavelength which is also commonly observed. There is also fluorescence at the wavelength longer than the 1050nm where absorption is quite small. Figure 6 (b) shows the ratio between the absorption and emission cross section (solid line) which agrees well with the observed tuning curve (broken line with open circles). By reducing the output coupling,

the laser oscillation was dominated by not the cavity loss but the absorption of the laser crystal itself. As a result, the laser oscillations were achieved in the broad wavelength region where absorption is small rather than in the region where the fluorescence is eminent. It is noted that we might be able to achieve the oscillation up to 1250nm which was not realized in the experiments due to the limited bandwidth of reflection of the cavity mirror.

It is also noted that the output power increased with the birefringent filter (BF) about three times as large as that without the BF. The maximum output power at 1030nm in a multimode oscillation was 498mW with 2290 mW pump power. The pump threshold of 832 mW, and slope efficiency of 36.5 % was obtained.
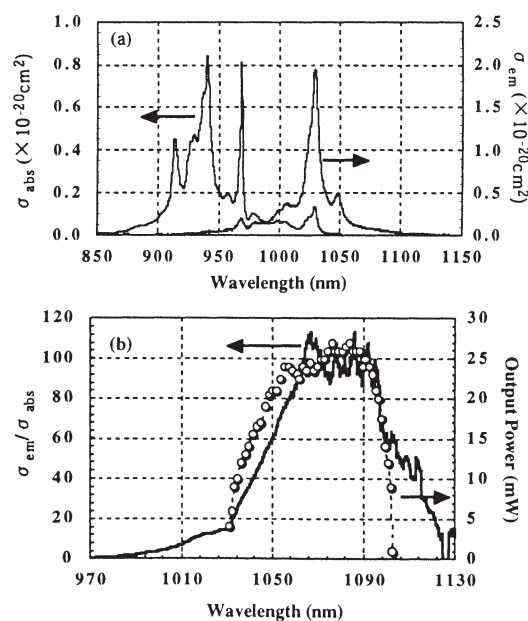

Fig.6 The absorption and the emission cross section of the Yb:YAG crystal used in the experiments : (a). The ratio between the absorption and emission cross section (solid line) and the tuning data shown in Fig.5 (broken line with open circles) : (b).

Fig.5 The tuning curves of the Yb:YAG laser using a 1-mm-thick quartz birefringent filter. The solid circles are tuning range with the output coupler reflectivity of 94 % and the solid triangles are with the output coupler reflectivity of > 99 %.

５．まとめ

　超短パルスレーザーを用いた加工の有用性を産業界で実用化するためのレーザーパラメーターを提案した。そのためのレーザー装置として LD 直接励起が可能で且つ超短パルスを発生しうるレーザー媒質である Yb:YAG の特徴に着目し、レーザー装置の試作を開始した。第一段階として、発振器を製作しその特性を調べた。波長可変性の測定に於いて、これまでに報告されたことのなかった広範囲の波長域を発見し、Yb:YAG が発振器としてのみならず LD 直接励起の増幅器に使用できる可能性を示した。

　今後、増幅器の設計・製作を行いシステム化し、LD 直接励起高繰り返し超短パルスレーザーの基礎技術を確立していく予定である。

References

1) B.N. Chichkov et al., Appl. Phys. Lett., A63 (1996) 1.

2) B. C. Stuart et al., CLEO'97 , Vol. 11, OSA Technical Digest Series, (1997) 159.

3) P. S. Banks et al., CLEO'98 , Vol. 12, OSA Technical Digest Series, (1998) 510.

4) B. Momma et al.,　Opt. Comm. 128 (1996) 101.

5) S. Nolte et al., CLEO'98 , Vol. 12, OSA Technical Digest Series, (1998) 510.

6) W. Koechner："Solid-State Laser Engineering", 4th Ed., Springer Series in Optical Sciences 1.

7) D. S. Sumida, T. Y. Fan: OSA Proc. Advanced Solid State Lasers, **20**, (1994) 100

8) U. Keller, K. J. Weinfarten, F. X. Kartner, D. Kopf, B. Braun, I. D. Jung, R. Fluck, C. Honninger, N. Matuschek, and J. A. der Au, IEEE JSTQE-**2** (1996) 435.

9) C. Honninger, I. Johannsen, M. Moser, G. Zhang, A. Giesen, U. Keller, Appl. Phys. B, **65,** (1997) 423

原 稿 受 付 日	平 成 12 年 9 月 25 日

Optics developments for CPA lasers in JAERI

Akira SUGIYAMA[*]and Hiroyasu FUKUYAMA
(Kansai Research Establishment, Japan Atomic Energy Research Institute)
Masamichi KATSURAYAMA and Yutaka ANZAI
(Corporate R&D center, Mitsui Mining & Smelting Co., Ltd.)

原研における CPA レーザー用光学結晶の開発

杉山　僚*、福山裕康 (日本原子力研究所　関西研究所)
桂山政道、安斎　裕 (三井金属鉱業株式会社　総合研究所)

Abstract

Nd:YAG crystal with a uniform doped ion concentration along its growth direction was successfully grown by a Czochralski growth furnace using a double crucible method.　The fluctuation of the concentration was less than 4%, nearly 1/4 of a Nd:YAG crystal grown by a conventional method.　Direct bonding without the use of any adhesives was also demonstrated on quartz glasses, YAG and Ti:sapphire laser crystals.　The bonded region of Ti:sapphire was evaluated from the macroscopic to the atomic level by three different methods of transmitted wavefront measurement, micro defects measurement and magnified inspection by a TEM.

1. Introduction

The ultra-short pulse and ultra-high peak power lasers have brought a new field called "super strong field science" which can be studied from sites of large laser facilities to normal size laboratories.[1],[2] This progress has been realized by the technique called CPA (Chirped Pulse Amplification)[3], supported by a solid laser system using neodymium doped yttrium aluminum garnet and titanium doped sapphire crystals which are exceptionally suitable laser materials for the realization of this advanced concept.　Recently, the demand of high intensity laser system is getting ever higher. The higher the requirement of the output intensity, the larger the crystals need to be.　For example, to establish a peta (10^{15}) watt class laser system, the main amplifiers require large laser crystals of Nd:YAG with over 250 mm in length and Ti:sapphire with over 80 mm in diameter, respectively.　It is formidably difficult to obtain such crystals having high optical quality and large enough to achieve stable and efficient high power laser generation since the crystals grown by conventional methods are often accompanied with defect formation and inhomogeneity of doped ions, depending on their small distribution coefficients in the crystals.　On the other hand, Ti:sapphire crystals in CPA lasers are normally used under the irradiation of extremely intense pumping and laser radiation of several

GW/cm^2 peak intensity, such conditions together with the nonlinear propagation of the laser beam frequently causes internal and surface fractures. Such problems forces users to recycle damaged crystals by cutting off the impractical portion of the crystals, polishing them, and bonding together the smaller crystals. From these points of view, we have studied to make large crystals with high optical quality by using two completely different methods.[4],[5] One of the methods is a Czochralski Nd:YAG crystal growth method using a double crucible linked with a continuous materials supplying system, and another method is a direct bonding method to obtain large laser crystals. We demonstrated this method to bond commercially available small laser crystals with high optical quality.[6] Here we report our recent progress in these developments. In the crystal growth of Nd:YAG, we have succeeded to grow the crystal with a total length of 185 mm with the uniform doped ion concentration along growth direction.[7] In the direct bonding of Ti:sapphire, the bonded region of 12 mm x 6 mm was evaluated from the macroscopic to the atomic level. The measurements were carried out by three different methods: (1) transmitted wavefront distortion measurements by a Fizeau interferometer; (2) micro defects measurements by a laser tomography method; (3) magnified inspections by a TEM (transmission electron microscope).

2. Nd:YAG crystal growth by a double crucible method

The intrinsic problem in a conventional Nd:YAG crystal growth using a single cylindrical crucible is the enlargement of Nd ion concentration along the growth direction, which is caused by a small distribution coefficient, a ratio of doped ion concentration captured in the crystal and in the melting material. In case of Nd:YAG, the factor is 0.17, smaller than 1.0, which causes a large amount of Nd ions accumulates in the crucible as the crystal grows. To cancel the dense concentration of Nd in the melting material and to create the uniform doped Nd:YAG crystal, we have proposed a double crucible method linked with the additional charge system. Fig. 1 shows a conceptual layout of our growth furnace. The YAG powder containing 0.58-at. % of Nd, leaner than melting material in the crucible, was additionally supplied by a feeder to the space between inner and outer walls of the crucible through an Ir pipe during the crystal growth. Since both melting materials stored in the space and inner crucible are linked through holes at the lower part of the inner cylindrical wall, the level of melt surface can be kept in uniform. It can restrict the change of the melt convection inside the crucible, which can reduce the fluctuation of growth condition and devise the stable crystal growth. In our method, the most significant problem in the development was a thermal shielding effect by the inner wall of the crucible. It forced to reduce the temperature gradient of 30 K/cm at the growth interface. As a result from optimization of insulator in the furnace, the gradient reached to almost the same steepness in case of using a single crucible, 70 K/cm, and Nd:YAG crystals with a total length of 185mm (straight part length of 110mm) was achieved in the growth condition of a crystal rotational speed of 15 rpm, a pulling rate of 0.5 mm/h and a material charging rate of 1.3 g/h, respectively. The fluctuation of doped ion concentration along the growth direction was less than 4 %, nearly 1/4 of the crystal grown by a conventional method, as shown in Fig.1.
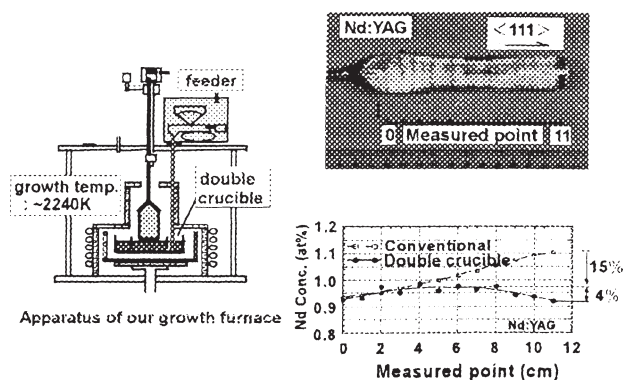
Figure 1 Nd:YAG crystal growth by the double crucible method.

3. Direct bonding process

Our bonding process was composed of five successive treatments, as shown schematically in Fig. 2. (a): After the specimens were polished to a flatness higher than 0.2 λ at 633 nm, the surfaces were prepared by several steps of chemical treatment to clean up and to form a hydrophilic (-OH) layer. (b): The wet specimens were brought to a clean ambient of class less than 10 to avoid contamination on the surfaces, and one of them was put on the other to contact gravitationally. (c): The new larger crystal was dried immediately in an atmospheric pressure oven at 473 K to get rid of excess water on the body of the crystal and to form hydrogen bonding at the contact interface. Hydrogen bonding

results from the reaction of OH + OH → H_2O + O. (d): The hydrogen bonded crystal was held by a graphite vice to apply low pressure in the direction perpendicular to the interface, which can prevent separation at the interface by thermal expansion of the specimen during the next heat treatment. Then, the crystal was brought to a high-temperature vacuum furnace for the bonding transformation from hydrogen bonding to the oxygen-bridged direct bonding by means of acceleration of dehydration condensation at 50 h and 1373 K. (e): The final stage was an annealing process to remove the optical distortion inside the crystal by placing the bonded crystal with no applied pressure at 10 h and 1373 K. In our bonding method, it is not necessary to use any adhesives and high pressure, which may lead to optical damage or distortion in the crystal. To achieve the bonding successfully, selection of etching chemicals and optimization of the chemical treatment in the process (a) were essential for each crystal. Detailed chemical treatment for Ti:sapphire and the desorption process of water in the high-temperature furnace have been described in a previous paper.[6] The bonded specimens composed of several types of laser crystals are shown in Fig. 3.

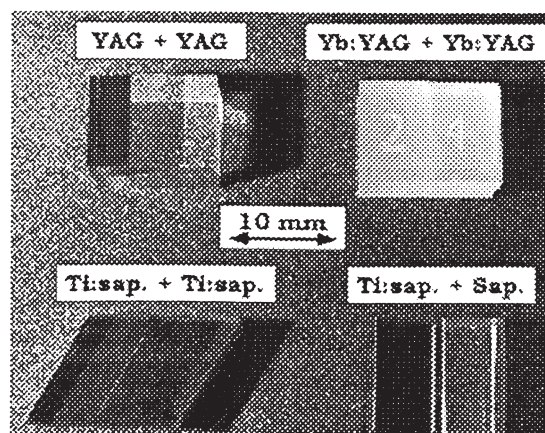Figure 2 Our direct bonding process

Figure 3 Direct-bonded laser optics.

4. Evaluation of the bonded region of Ti:sapphire

To evaluate the bonded region of 0.15-wt. % Ti:sapphire crystal with a bonding surface dimension of 12 x 6 mm^2, we made three different measurements from the macroscopic to the atomic level as follows.

4.1. Transmitted wavefront distortion

To devise accurate measurements with a Fizeau interferometer (Zygo: GPI-XP), the bonded crystal was located on the narrow space between transmission and reference flat mirrors to reduce the interference fringe motion by the fluctuation of airflow. Since the measured wavefront data in this system implies the roughness of the polished surfaces and distortion of the bonded region as well as inhomogeneity inside the specimen, other single Ti:sapphire crystals, having the same surface flatness of over 0.1 λ at 633 nm on both Brewster's ends and a different length of 8 mm and 18 mm, were also measured to estimate the crystal inhomogeneity. The transmitted wavefront of the bonded crystal with a length of 14 mm was 0.152 λ at 633 nm in the area of 10 mm x 5 mm square. The estimated inhomogeneity was 0.037 λ/cm at 633 nm from the measurements of the other crystals, and it was assumed that the transmitted wavefront of the single crystal having with the same length as the bonded one was 0.121 λ at 633 nm. As a result, the wavefront distortion by the bonded region was 0.031 λ at 633 nm.

4.2. Micro defects measurements

Laser tomography has been used as one of the attractive non-destructive methods to detect micro defects in crystals by means of optical scattering.[8],[9] Our laser tomography system (Mitsui: MO-421) consists of an optical unit and a data analyzer. In the optical unit, the bonded specimen located on a 3-D

motion variable stage was irradiated by a probe laser of the 2nd harmonic of CW Nd:YAG. The focused probe laser beam on the specimen was about 10μm in diameter. Optical scattering signals generated from defects inside the specimen were vertically detected by a CCD camera through an optical microscope. A color glass filter was inserted between the CCD camera and the microscope to avoid the effect of fluorescence in the scattering measurements. In Fig. 4, small spots appearing horizontally inside the oval shows the micro defects existing on the bonded surface, and the other spots spread through the whole image were intrinsic defects formed in the crystal growth. It can be seen that the number of micro defects on the bonded surface are much smaller than that of the intrinsic ones, which suggests that the optical loss at the bonded region of Ti:sapphire was insignificant and the bonded crystal was applicable for laser oscillation.
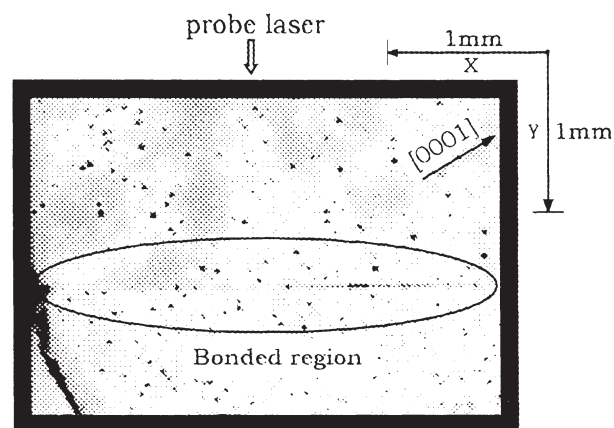

Figure 4 Micro defects around the bonded region.

4.3. Magnified inspections in atomic level

The bonded region was also inspected by a field emission TEM (Hitachi: HF-2000) at a magnification power of 4-million. In the measurements, additional fabrication using argon ion milling was required to prepare a specimen extracted from the bonded

Ti:sapphire that was already used for the impact fracture test. Thickness of the specimen was reduced to around 70 nm in the bonded area. A probe electron beam accelerated by 200 kV was used for TEM measurements. Fig. 5 shows the magnified image of bonded region. Although obscure parts of 1 nm size slightly appeared along the bonded interface, the atoms in the bonded region were well arranged with the same regularity as inside the crystal. It seemed that the obscure parts were based on the irregularity of the polished surfaces of the Ti:sapphire crystals. In the bonding process, most of the irregularity would be reduced by elastic deformation and diffusion of the atoms during the long heat treatment while the rest of irregularity could be less deformed by these effects.
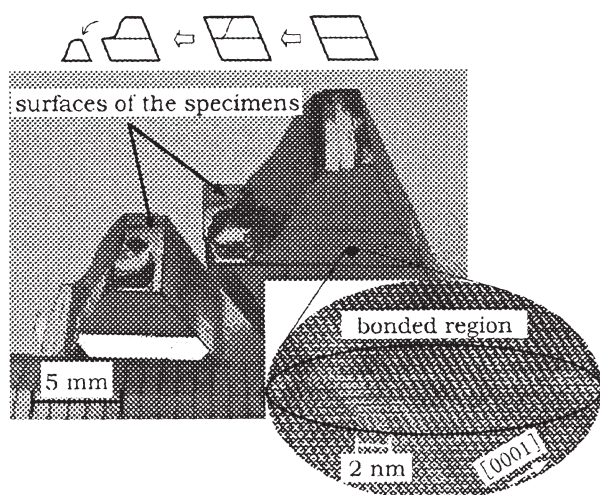
Figure 5 Magnified image of bonded Ti:sapphire.

5. Conclusion

To achieve the uniform Nd doped ion concentration in Nd:YAG single crystals, we proposed the double crucible crystal growth method linked with the successive material supplying system. As a result from optimization of insulator in the furnace, the temperature gradient reached to 70 K/cm and Nd:YAG

crystals with a total length of 185mm was achieved.

The direct bonding of several types of laser crystal was also demonstrated. The bonded region of Ti:sapphire was evaluated from the macroscopic to the atomic level by three different methods such as transmitted wavefront distortion measurements by the interferometer, micro defect measurements by laser tomography and magnified inspections by TEM. From the first interferometer experiments, the wavefront distortion caused by the bonded area of 10 mm x 5 mm was estimated at 0.031 λ at 633 nm. The second micro defect measurements showed the number of micro defects on the bonded region were much smaller than that of the intrinsic ones inside the crystal. It suggests the previous results of optical inspection and laser oscillation in ref. 6. From the third inspections, the atoms in the bonded region were well arranged with the same regularity as inside the crystal although obscure parts 1 nm in size appeared slightly along the bonded interface.

References

(1) M. Kando, H. Ahn, H. Dewa, H. Hosokai, T. Ueda, m. Uesaka, T. Watanabe, H. Nakanishi, A. Ogata and K. Nakajima, "Experimental results of laser wakefield acceleration using a femtosecond Terawatt laser pulse," *Jpn. J. Appl. Phys.* **38**, pp. L967-L969, 1999.

(2) M. Kado, T. Kawachi, N. Hasegawa, M. Tanaka, K. Sukegawa, A. Nagashima, A. Sasaki and Y. Kato, "Transient collisional excitation X-ray laser generation with pico-second laser pulses," *7th Inter National conference on X-ray lasers*, **abstract O3**, pp. 7, Saint-Malo, France, 18th -23rd June, 2000.

(3) D. Strickland and G. Mourou, "Compression of amplified chirped optical pulses," *Opt. Commun.*, **56**, pp. 219-221, 1985.

(4) A. Sugiyama, Y. Anzai, M. Katsurayama, T. Yamazaki, K. Yamagishi, T. Sasuga, T. Arisawa and H. Takuma, "Studies of laser crystal growth," *JAERI-Tech.*, **97-049**, 1997.

(5) A. Sugiyama, H. Fukuyama, M. Katsurayama, Y. Anzai and S. Nagai, "Development of high quality large laser crystals for a CPA laser system," *JAERI-Conf.*, **2000-006**, pp. 71-74, 2000.

(6) A. Sugiyama, H. Fukuyama, T. Sasuga, T. Arisawa and H. Takuma, "Direct bonding of Ti:sapphire laser crystals," *Appl. Opt.*, **37**, pp. 2407-2410, 1998.

(7) M. Katsurayama, Y. Anzai, A. Sugiyama, M. Koike and Y. Kato, "Growth of neodymium doped YAG single crystals by a double crucible method," *The 1st Asian Conference on Crystal Growth and Crystal Technology*, **abstract T-P-69**, pp. 481, Sendai, Japan, 29th August – 1st September, 2000.

(8) K. Moriya, "Light scattering from defects in crystals: scattering by dislocations," *Philosophical Magazine*, **B64**, pp. 425-445, 1991.

(9) H. Fukuyama and A. Sugiyama, "Density measurements of micro defects inside optical materials using a laser tomography method," *JAERI-tech.*, to be published.

Nd:YAG セラミックスレーザーにおける熱複屈折効果

庄司 一郎 *，佐藤 庸一，栗村 直，平等 拓範 (分子科学研究所)
池末 明生 (ファインセラミックスセンター)　吉田 國雄 (大阪工業大学)

Thermal Birefringence in a Ceramic Nd:YAG Laser

Ichiro Shoji, Yoichi Sato, Sunao Kurimura, and Takunori Taira (Institute for Molecular Science)
Akio Ikesue (Japan Fine Ceramics Center)　Kunio Yoshida (Osaka Institute of Technology)

Abstract

We have investigated optical properties, laser performances, and thermal properties of recently developed Nd:YAG ceramics with Nd^{3+} concentration up to 6.6 at. %. Absorption coefficient increases linearly with Nd^{3+} concentration, which enabled a microchip of 3.4 at. % Nd:YAG ceramic to oscillate with 2.3 times higher output than that from a conventional single-crystal microchip. The loss of a 2.3 at. %-doped ceramic is as low as that of a single crystal. Thermal birefringence of the ceramics is the same with that of single crystals at the same Nd^{3+} concentration, and the birefringence becomes larger as Nd^{3+} concentration increases.

キーワード: セラミック YAG，マイクロチップレーザー，Nd:YAG，熱複屈折
(ceramic YAG, microchip laser, Nd:YAG, thermal birefringence)

1 INTRODUCTION

Diode-pumped microchip solid-state lasers are attractive light sources characterized by compactness, high efficiency, and a small number of longitudinal and low-order transverse modes.[1] A wide variety of materials has been investigated to develop higher power and more efficient microchip lasers.

We have recently developed highly Nd^{3+}-doped polycrystalline YAG ceramics that have transparency comparable to Nd:YAG single crystals.[2],[3] The highly Nd^{3+}-doped ceramic YAG is a promising material for high-power and high-efficiency microchip lasers because it has both advantages of a conventional Nd:YAG single crystal which has good thermo-mechanical properties and $Nd:YVO_4$ which has large absorption coefficients. Moreover, these ceramics can be made in much shorter time compared with single crystals;

it takes only a few days for ceramics using the sintering process, while typically a few months for single crystals by the Czochralski method. The Nd^{3+} concentration in the ceramic YAG samples was confirmed with an electron probe microanalyzer (EPMA; Shimadzu Model 8705), and from 0 to 8.7 at. %-doped samples have been obtained to date.

We investigated optical properties, laser performances,[4],[5] and thermal properties of the Nd:YAG ceramics.

2 OPTICAL PROPERTIES

Figure 1 shows the absorption spectra of 2.0, 3.4 and 6.6 at. % Nd:YAG ceramics and a 1.0 at. %-doped single crystal at a 0.2 nm resolution. The highly Nd^{3+}-doped YAG ceramics had large absorption coefficients, which increased linearly with the Nd^{3+} concentration. The fluorescence
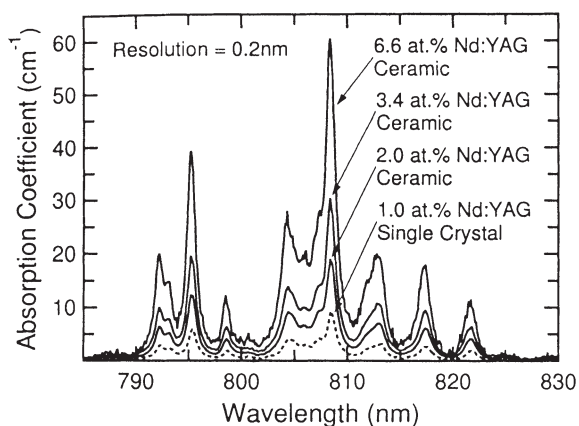
Fig. 1. Absorption spectra of 2.0, 3.4, and 6.6 at % Nd:YAG ceramics (solid curves), and 1.0 at % Nd:YAG single crystal (dashed curve).
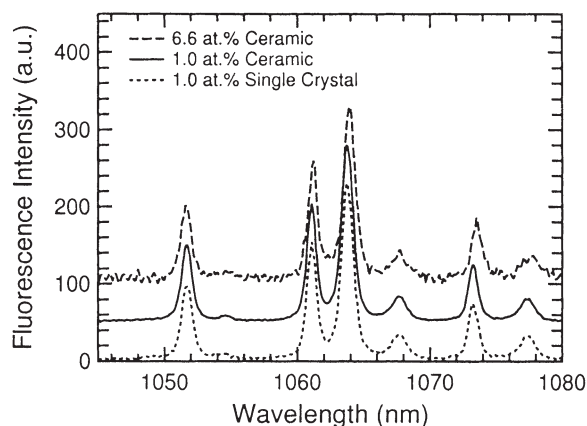

Fig. 3. Fluorescence spectra of 1.0 and 6.6 at.% Nd:YAG ceramics and a 1.0 at.% Nd:YAG single crystal. The graphs are offset to be clearly distinguished each other.
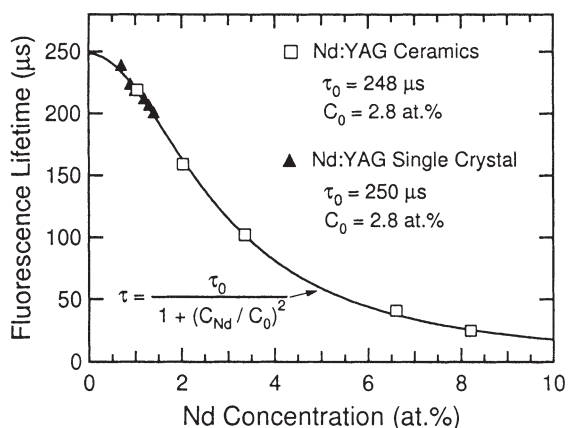

Fig. 2. Fluorescence lifetime versus Nd^{3+} concentration. The open squares show the experimental data for the Nd:YAG ceramics, and filled triangles those for the Nd:YAG single crystals. The solid curve is the fitting with the inset equation.

6.6 at. %-doped ceramic had 0.2 nm longer peak wavelengths than the 1.0 at. %-doped samples. The full width at half maximum was 1.0 nm for every sample.

We have succeeded in microchip laser oscillation and obtained more than two times higher output power from a microchip of a 3.4 at.% Nd:YAG ceramic than from a same sized microchip of a Nd:YAG single crystal at the same input power.[4] We estimated the cavity losses using the following equation

$$ L_i = \frac{(T_2/T_1)T_1 - (\eta_2/\eta_1)T_2}{\eta_2/\eta_1 - T_2/T_1}, \qquad (1) $$

where η_i's and T_i's are the slope efficiencies and the transmittances of the output couplers, re-

lifetime as a function of the Nd^{3+} concentration is shown in Fig. 2. The pump wavelength and the pump width were 808 nm and 10 ns, respectively. It was found that the ceramics and the single crystals had nearly the same τ_0, ~ 250 μs, and the same quenching parameter C_0, 2.8 at. %.

Figure 3 shows the fluorescence spectra of 1.0 and 6.6 at. % Nd:YAG ceramics and a 1.0 at. % Nd:YAG single crystal measured at room temperature. The spectra of the 1.0 at. %-doped ceramic and single crystal were identical, while the

Table 1. Slope Efficiencies and Cavity Losses[a]

Nd Concentration (at. %)	η_1 (%)	η_2 (%)	L_i (%)	α_i (cm^{-1})
Single Crystal				
0.9	20.7	15.7	0.5	0.04
Ceramics				
2.4	24.7	19.0	0.5	0.03
4.8	27.4	13.7	2.2	0.13

[a]Loss Coefficient

spectively. As summarized in Table 1, the loss of the 2.3 at. % ceramic was found to be as low as that of the single crystal. On the other hand, the 3.4 at. %-doped ceramic had much higher loss coefficient. It is presumably because the scattering loss at the grain boundaries becomes significant since the ceramics with higher Nd^{3+} concentration have smaller grain sizes, i.e., the increased number of the grain boundaries.[3]

3 THERMAL PROPERTIES

3.1 Thermal Conductivity

Thermal conductivity was measured with the laser flash method from room temperature to 300 °C.[6] Figure 4 shows, as an example, the dependence of thermal conductivity on the Nd^{3+} concentration measured at 20 °C. It was found that the thermal conductivity of the ceramic YAG was as high as that of a YAG single crystal, which was twice that of $Nd:YVO_4$, and hardly degraded even at higher Nd^{3+} concentration. This property is preferable for high power operation to maintain the highly efficient oscillation in microchip structures.

3.2 Thermal Birefringence

We measured thermal birefringence of Nd:YAG ceramics by the pump-probe experiment. Figure 5 schematically shows the experimental setup. A Ti:Sapphire laser oscillating at 808 nm was used as the pump beam. The maximum input power was 3 W. The pump beam was focused onto the sample with the radius of 80 μm. On the other hand, a He-Ne laser was used as the probe beam. After the probe beam was polarized parallel to Y direction with a polarizer, it passed through the sample, reflected at the plane surface of the focusing lens, and went back through the sample again. A part of it was reflected at the beam splitter, and only the depolarized (X-polarized) component of the probe beam transmitted the analyzer which was in the cross-nicol configuration with the polarizer. Passing through a filter which absorbed the pump beam, the depolarized beam pattern was observed with a CCD camera or its power was measured with a photodetector.

In an isotropic (space group O_h) crystal such as YAG, thermal birefringence occurs between the radial and the azimuthal directions in a plane perpendicular to the direction of the beam propagation, as depicted in Fig. 6.[7] Hence the depolarized beam which transmitted the analyzer

Fig. 4. Thermal conductivity of YAG ceramics as a function of Nd^{3+} concentration at 20 °C. The data of YAG single crystal and YVO_4 are also shown.
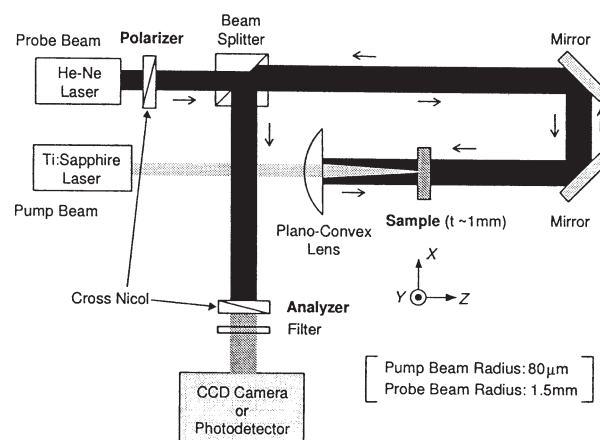

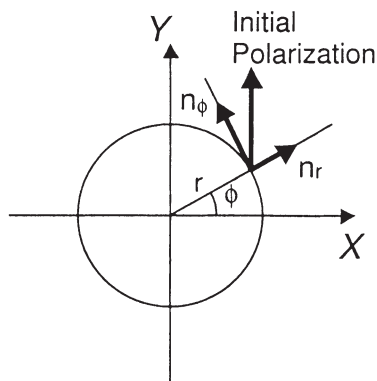Fig. 5. Experimental setup for the thermal birefringence measurement.

Fig. 6. Orientation of the indicatrix: radial and azimuthal refractive indices, n_ϕ and n_r, in a plane perpendicular to the direction of the beam propagation.
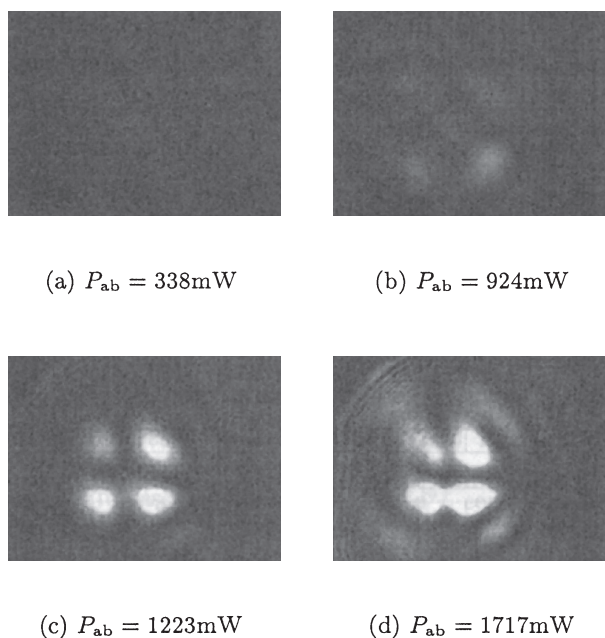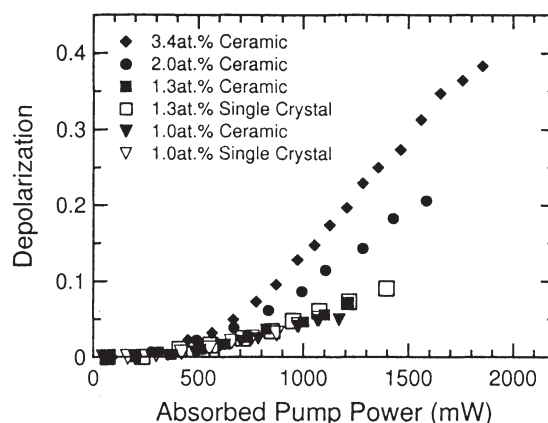

Fig. 8. Dependence of the depolarization on the absorbed pump power for the ceramic and the single-crystal samples with various Nd^{3+} concentration.
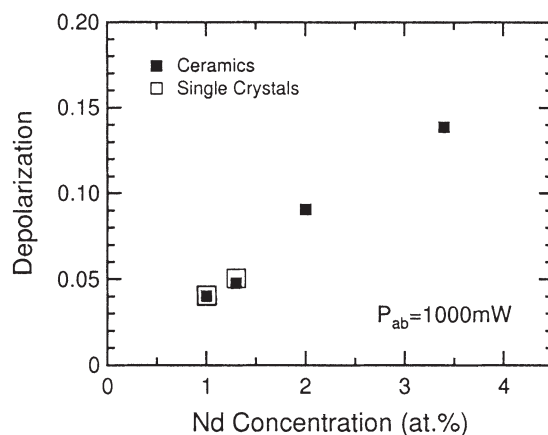

(a) $P_{ab} = 338$mW

(b) $P_{ab} = 924$mW

(c) $P_{ab} = 1223$mW

(d) $P_{ab} = 1717$mW

Fig. 7. Images of the depolarized beam from the 1.3 at. % Nd:YAG ceramic sample, which were observed with the CCD camera at the absorbed pump power P_{ab}.

Fig. 9. Depolarization as a function of the Nd^{3+} concentration for the ceramic and the single-crystal samples at the absorbed pump power of 1000 mW.

makes the images shown in Fig. 7. Although the image was not seen at low absorbed pump power (Fig. 7(a)), it got clearer as the absorbed pump power increased, and the thermal lens effect distorted the image at higher absorption (Fig. 7(d)).

If the depolarization is defined by the ratio of the depolarized power to the total probe power as $P_\perp/(P_\| + P_\perp)$, dependence of the depolarization

on the absorbed pump power for the ceramic and single-crystal samples with various Nd^{3+} concentration is shown in Fig. 8. On the other hand, Fig. 9 shows the depolarization as a function of the Nd^{3+} concentration at the absorbed pump power of 1000 mW.

We found that the ceramic and single-crystal YAG have the same depolarization when the Nd^{3+} concentration is same. It means that the effect of the thermal birefringence is same between the ceramic and single-crystal YAG. This fact is attributed to the isotropy of the YAG crys-

tal. Koechner and Rice calculated the amount of the thermal birefringence induced in a Nd:YAG rod which had a cylindrical symmetry along the [111] direction.[7] They obtained the thermal birefringence Δn as

$$\begin{aligned} \Delta n &= n_\phi - n_r \\ &= \frac{n_o^3}{2}(P_{11} - P_{22})(\varepsilon_r - \varepsilon_\phi) \end{aligned} \quad (2)$$

where n_o is the initial refractive index, P_{11} and P_{22} are the photoelastic coefficients, and ε_r and ε_ϕ are the radial and the azimuthal strain tensors, respectively. Equation (2) does hold not only for [111] but any direction in an isotropic crystal such as YAG.[8] Although the ceramic YAG consists of 10–100 μm-sized YAG single crystals which orient in various directions, the isotropy of YAG crystal makes the thermal birefringence unchanged in the ceramic YAG. It is noted that we assume the thermally induced strains in YAG ceramics should be the same with that in single crystals, which we have to investigate by further work.

Moreover, it was also found that the depolarization became larger in samples with higher Nd^{3+} concentration even if the same pump power was absorbed. This is because the thermal distribution in the sample is different for different Nd^{3+} concentration. Figure 10 schematically shows the difference between the samples with higher and lower Nd^{3+} concentration. In the case of end pumping, the sample with higher Nd^{3+} concentration localizes the heat near its surface because it has larger absorption coeffi-
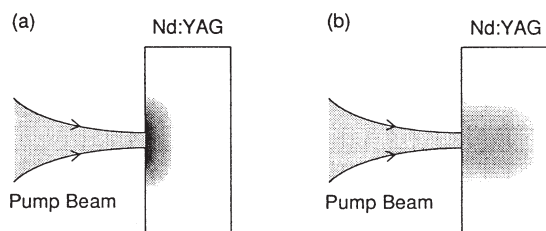
Fig. 10. Thermal distribution in the samples with (a) higher and (b) lower Nd^{3+} concentration.

cient or shorter absorption length. This localized heat induces stronger strain than that in the sample with lower Nd^{3+} concentration even if the total heat is the same in both the samples, which results in larger thermal birefringence. It is an undesirable feature of a microchip laser using highly Nd^{3+}-doped YAG ceramics, but nevertheless the thermal effect can be smaller than that of $Nd:YVO_4$ since the thermal conductivity of YVO_4 is only as half as that of YAG. Moreover, a composite YAG ceramics with Nd^{3+}-doped and undoped region can be made easily, which would greatly reduce the thermal effects.

4 CONCLUSION

Optical properties, laser performances, and thermal properties of Nd:YAG ceramics have been investigated with Nd^{3+} concentration up to 6.6 at. %. The absorption coefficient increased linearly with Nd^{3+} concentration, and the quenching parameter was the same with that of single crystals. 2.3 times higher output was obtained from the microchip of a 3.4 at. % Nd:YAG ceramic than that from a conventional single-crystal microchip. The loss of a 2.3 at. %-doped ceramic was as low as that of a single crystal. While thermal birefringence of the ceramics was the same with that of single crystals at the same Nd^{3+} concentration, the birefringence became larger as Nd^{3+} concentration increased. We have to investigate the thermal effects in composite YAG ceramics with Nd^{3+}-doped and undoped region, which can be made easily with the sintering process and is expected to greatly reduce the thermal effects. It is concluded that the Nd:YAG ceramics are promising as high power and highly efficient microchip laser materials.

5 ACKNOWLEDGMENT

REFERENCES

(1) J. J. Zayhowski and A. Mooradian, Opt. Lett. **14,** 24 (1989).

(2) A. Ikesue, T. Kinoshita, K. Kamata, and K. Yoshida, J. Am. Ceram. Soc. **78,** 1033 (1995).

(3) A. Ikesue, K. Kamata, and K. Yoshida, J. Am. Ceram. Soc. **79,** 1921 (1996).

(4) I. Shoji, S. Kurimura, Y. Sato, T. Taira, A. Ikesue, and K. Yoshida, Appl. Phys. Lett. **77,** 939 (2000).

(5) T. Taira, A. Ikesue, and K. Yoshida, OSA Trends in Optics and Photonics *Vol 19, Advanced Solid-State Lasers,* W. R. Bosenberg and M. M. Fejer, eds. (Optical Society of America, Washington, DC 1998), 430–432 (1998).

(6) T. Taira, S. Kurimura, J. Saikawa, A. Ikesue, and K. Yoshida, OSA Trends in Optics and Photonics *Vol 26, Advanced Solid-State Lasers,* M. M. Fejer, H. Injeyan, and U. Keller eds. (Optical Society of America, Washington, DC 1999), 212 (1999).

(7) W. Koechner and D. K. Rice, IEEE J. Quantum Electron. **QE-6,** 557 (1970).

(8) I. Shoji, S. Kurimura, T. Taira, in preparation.

Solid State Lasers and Nonlinear Tunable Sources: 2000

Robert L. Byer (Stanford University)

Abstract

 Advances in laser diode pumped solid state lasers and tunable sources for atmospheric remote sensing and spectroscopy are discussed. Topics include laser diode pumped solid state lasers, slab lasers, and recent advances in edge-pumped slab lasers. Advances in laser sources have led to advances in tunable frequency sources in both birefringent and quasi-phasematched nonlinear crystals. Tunable infrared in parametric oscillator-amplifiers have enabled remote sensing of atmospheric molecules in the near infrared. Future directions of laser sources and tunable devices will be illustrated by global remote sensing applications that lie in the future.

原稿受付日	平成 12 年 10 月 2 日

等方性石英ガラスにおける二次非線形光学性

亀山 晃弘*、横谷 篤至、黒澤 宏

（宮崎大学工学部）（分子科学研究所）

Second-Order Optical Nonlinearity in Isotropic Silica Glass

Akihiro Kameyama and Atsushi Yokotani (Faculty of Engineering, Miyazaki University)

Kou Kurosawa (Institute of Molecular Science),

Abstract

We have demonstrated large second-order optical nonlinearity is generated in thermally poled high-purity silica glass that is exposed to KrF excimer laser pulses before the poling. The maximum $\chi_{33}^{(2)}$ value of 0.71pm/V is observed in the sample which is annealed to 900°C in air and O_2 molecules are introduced in. KrF excimer laser pulses erase the nonlinearity induced in the glasses. Based on these findings and optical absorption and luminescence, we show that point defects of $\equiv$Si-O⁻ play a key role for the nonlinearity formation in the poled high-purity silica glass.

キーワード：シリカガラス、２次非線形光学性、熱ポーリング、KrF エキシマレーザー照射
(Silica glass, Second-order optical nonlinearity, thermally poling, KrF excimer laser irradiation)

1 はじめに

石英ガラスは光を主役とする最先端技術時代にあって最も重要な材料となっている。ガラスは本来、反転対称性を有するために２次非線形誘電感受率$\chi^{(2)}$の値が０であり、原理的には第２高調波(SHG)は生じない。しかしながら、石英ガラスに熱ないしは紫外光と同時に高電圧を印加するポーリングによって、かなり大きな２次非線形光学性を付加でき、レーザー光の波長変換素子や電気光学スイッチ等に応用できることから、注目を集めるようになった[1-5]。実際 Ge を添加した光ファイバーに熱ポーリングをおこなうことにより 20％以上の波長変換を達成した例も報告されている[6]。また、２次非線形光学性の発現メカニズムの解明についても精力的におこなわれている。従来電圧印加によってガラス中の誘起双極子が配向するとの説と、空間電荷場が誘起され、ガラスが本来持っている$\chi^{(3)}$を通して発現するとの説の２つがあった。発現する$\chi^{(2)}$の大きさや、熱ポーリングに置いては大きな$\chi^{(2)}$をもつ領域が、試料がポーリング時に陽極と接触していた表面近傍わずか 10μm 程度の厚さに局在していることから、後者のメカニズムが妥当であると考えられるが、まだ明確ではない。更に発現が確認されているガラスでは金属イオンや希土類イオンといった元素ないしは不純物が不可欠であり、第３原子に付属する欠陥が起因していると考えられる。一方、純粋な石英ガラスにポーリングをおこなっても$\chi^{(2)}$は発現しない。我々は以前から純粋な石英ガラスに X 線あるいは紫外レーザーを照射して欠陥を誘起し、それによって$\chi^{(2)}$が発現することを明らかにしてきた[7]。

今回は、紫外レーザー光が、$\chi^{(2)}$を誘起することと、更に発現した$\chi^{(2)}$を消滅することになる結果から、$\chi^{(2)}$に関する結果の同定、$\chi^{(2)}$が$\chi^{(2)}\times Edc$によって生じること、及び非架橋酸素欠陥(NBO-, non-bridging oxygen, SiO-) が$\chi^{(2)}$生成に不可欠であることを見いだしたので報告する。

2 実験

2－1 試料

試料には四塩化珪素($SICl_4$)を酸水素炎中で加水分解する方法で作成した石英ガラスを用いた。試料には金属イオンはほとんど存在しないが、H_2、O_2、H_2O 分子、及び Si-OH 構造が含まれている。試料中の H_2 と O_2 分子の量は酸水素炎中の O_2 と H_2

の濃度を変えることによって調整できる。濃度比が $H_2/O_2 < 2$ の条件下で作成された試料では O_2 分子が大量に含まれ、逆に $H_2/O_2 > 2$ の条件下で作成された試料では H_2 分子が大量に含まれる。OH 濃度は四塩化珪素を酸水素炎中に投入する量を変化させることによって調整することが可能である。今回、試料中の H_2 と O_2 濃度を測定しなかったが、OH 濃度については赤外分光装置を用いて波数 3600cm^{-1} での吸収スペクトルを測定して見積もった。使用した試料は便宜上、O_2 と H_2 と OH 濃度別に分類して、試料(A)：O_2 過多、OH=1200ppm、試料(B)：H_2 過多、OH=1200ppm、試料(C)：H_2 過多、OH=550ppm とした。試料の作成条件等を表１にまとめた。

試料は直径 20mm、厚さ 1.5mm で表面は光学研磨した。

また試料中の O_2 を調整するため、空気中、又は He 雰囲気中で熱処理を行った。空気中で熱処理をおこなうことにより試料には O_2 分子が導入される。一方、He 雰囲気中で熱処理をおこなうことにより O_2 分子が排出される。我々は１気圧の空気と He 中で 900℃ で２時間で熱処理を行った。

試料に欠陥を導入するため、熱ポーリング前に KrF エキシマレーザー（波長 248nm、パルス幅 20ns）を照射した。後述するが、試料には電圧印加のために金スパッタ膜を堆積させていたので、その金スパッタ膜をとおしてレーザー照射を行った。照射強度は集光レンズ（焦点距離 72mm）を用いて試料—レンズ間の距離を変化させることで、0.6〜60mJ/cm^2 の範囲内で変化させた。熱ポーリングは紫外レーザー照射後３分以内に行った。

また、紫外レーザー照射によって、一度作成した２次非線形光学相が消去される。その照射強度依存性を測定するため、熱ポーリングの後に照射実験を行った。また波長依存性を調べる目的で、Nd:YAG レーザーの第２高調波（波長 532nm、パルス幅 7ns、照射強度 60mJ/cm^2）を照射した。

2−2　熱ポーリング

我々は以下の手順で熱ポーリングをおこなった。まず試料表面にスパッタ法で厚さ 100nm、直径 8mm の金膜を堆積させた。次に試料を２つの金属電極で挟みつけ、試料両端（厚さ 1.5mm）に 4.5kV の直流電圧を印加した。印加した状態で試料を 260℃ の温度まで 10℃/min で昇温し、20 分間維持した後、10℃/min で降温した。室温に戻った段階で電圧をゼロにし、金スパッタ膜を除去した。

2−3　$\chi^{(2)}$ 測定

試料の２次非線形誘電感受率 $\chi_{33}^{(2)}$ を求めるために、我々は Q スイッチ動作の Nd:YAG レーザーの基本波（波長 1064nm、パルス幅 7ns、p 偏光)を試料に照射して得られた第２高調波(SHG)を測定した。レーザー光はレンズ（焦点距離 150mm）を使って

ビーム径 100μm、ピーク強度 0.4MW/cm^2 で試料表面に集光した。基本波光と Q スイッチ動作で用いられるポッケルスセルからでる SHG 光を分離するため、レーザー装置の出射口に分散プリズムを置いた。試料から得られた SHG 光は再集光レンズ（焦点距離 90mm）と赤外フィルターを通した後、分光器で単色化してから光電子増倍管（浜松ホトニクス社製 R105）で検出した。得られた電気信号はピークホールド回路に通した後、AD コンバータを介してパーソナルコンピューターで記録した。測定は１０回行い平均化した。SHG 信号強度の入射角依存性を調べるため、試料は-60〜60° まで 1°おきに回転させた。熱ポーリング石英ガラスの $\chi_{33}^{(2)}$ を求めるにあたって、我々は次のような仮定を追いた。まず試料表面に対して法線方向を z 軸とした。また２次非線形光学相の厚さが厳密には分からないので、ガラスに対する Nd:YAG レーザーの基本波と第２高調波とにおける屈折率から決まる相互作用長 22μm を２次非線形光学相の厚さとした。また SHG 測定装置の感度を校正するため a-水晶を参照試料（$\chi_{11}^{(2)}$=0.72pm/V）として用いた[8]。

3　実験結果

表１に３種類の試料にそれぞれ処理を行った際に発現した $\chi_{33}^{(2)}$ の値を示す。通常の熱ポーリングを行った場合（KrF エキシマレーザー照射を行わない。）、高純度石英ガラスから２次非線形光学性は発現しなかった。次にあらかじめ KrF エキシマレーザー照射をおこなってから熱ポーリングを行うことにより、試料(A)から２次非線形光学性が発現した。一方、試料(B)と(C)からは観測できなかった。図１にあらかじめ KrF エキシマレーザーを照射し、それから熱ポーリングした試料(A)の $\chi_{33}^{(2)}$ の値をレーザーパルス数に対してプロットしてある。レーザー照射がなければ 0 である $\chi_{33}^{(2)}$ がわずか 100shots を照射するだけで 0.25pm/V になることが分かる。その $\chi_{33}^{(2)}$ 値は 1000shots 程度までは急激に増加し、その後緩やかに増加した。そして 15000shots 照射後では 0.51pm/V に達した。

次にこの試料(A-1)を空気中で熱処理し、O_2 分子を導入した。その後 KrF エキシマレーザーを照射してから熱ポーリングして作成した試料(A-2)の場合、先の場合と比べると、$\chi_{33}^{(2)}$ の値がいずれの shots 数でも大きくなっており、15000shots で 0.71pm/V になった。しかし $\chi_{33}^{(2)}$ の値の照射数に対する変化は熱処理せずの場合と変わらなかった。

同様に試料(A-2)を He 中で熱処理して、O_2 分子を排出して作成した試料(A-3)の場合、レーザー照射を行ってから熱ポーリングを行うと $\chi_{33}^{(2)}$ が発現したものの、その値は試料(A-1)の場合よりも小さくなった（表１)。

次に試料(B)を見てみると前述したように、試料(A)とは異なり、熱ポーリングに先駆け UV レーザーを照射しても（試料(B-1)）$\chi_{33}^{(2)}$ は観測できなかった。次に空気中で熱処理を行って O_2 分子を導入することにより（試料(B-2)）$\chi_{33}^{(2)}$ が発現したが、その値

はわずか 0.03pm/V 程度であった。一方、この試料(B-2)を He 中で熱処理を施すことにより（試料(B-3)）、$\chi_{33}^{(2)}$は 0.27pm/V にまで増大した。

試料(C)については上記の2種類の試料と全く違う振る舞いをし、熱処理を行っても全く2次非線形光学性は発現しなかった。以上のことから KrF エキシマレーザー照射による純粋石英ガラスの2次非線形光学性発現には O_2 分子と OH が必要であることが分かった。
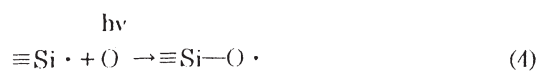
次に熱ポーリングして$\chi_{33}^{(2)}$の発現した試料(A-1)に照射強度 60mJ/cm² で KrF エキシマレーザーを照射して、その時の$\chi_{33}^{(2)}$の変化を図2にプロットした。図2には、レーザー照射時に見えられる 1.9eV の赤色の蛍光強度も同時にプロットした。$\chi_{33}^{(2)}$は少ない shots 数で極めて早く減少し、僅か 500shots 程度で$\chi_{33}^{(2)}$はほぼ0になった。同時に 1.9eV の赤色蛍光強度も照射に対して、$\chi_{33}^{(2)}$の減少とほぼ同様の傾向を示した。1.9eV の蛍光には$\equiv$Si-O・ (non-bridging oxygen hole center、NBOHC) が関係していることが報告されており[9]、KrF excimer laser 照射によって石英ガラス中に$\equiv$Si-O・に関係する欠陥を消去することによって$\chi_{33}^{(2)}$が減少していることが明確となった。そこで次に2次非線形光学性の消失の反応メカニズムを明らかにするために$\chi_{33}^{(2)}$の減少のレーザー強度依存性を調べた。表2は最初の$\chi_{33}^{(2)}$から 1/e まで減少する shots 数を 0.6、6、60mJ/cm² の各照射強度において、まとめたものである。各照射強度における shots 数と照射強度の積がほとんど同じであることが分かる。すなわち$\chi_{33}^{(2)}$の消失は1光子過程であることが分かった。一方、比較のため Nd:YAG レーザーの第2高調波を 60mJ/cm² の強度で照射したところ、5000shots 照射しても$\chi_{33}^{(2)}$の値には全く変化が見られなかった。このことより紫外光が$\chi_{33}^{(2)}$消去に不可欠であることが分かる。

4 考察

純粋石英ガラスに紫外エキシマレーザーを照射した際に起こる光化学反応についてはいくつかの詳細な研究がなされている[10-12]。酸水素炎中で四塩化珪素を加水分解して作成した試料の場合、大量の H_2O 分子が Si-OH 構造と水素結合によって結びついている。この構造は高温では式（1）の右側の構造に変化する確率が高くなる。

$$\equiv Si-O-H \rightarrow \equiv Si-O\cdots H \rightarrow \equiv Si \quad O \quad H \quad (1)$$
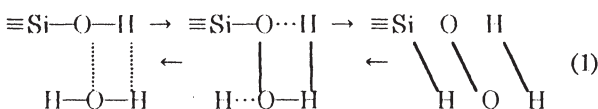
ここで…は水素結合を示している。KrF エキシマレーザーを照射することにより$\equiv$Si-H は$\equiv$Si・ (E-center) と H に分離し、また O_2 分子は 2O に分離する。もし試料中に O_2 分子が大量にあるのであれば、式（2）から（4）に示しているように $\equiv$Si-O・が生成される。

$$\equiv Si-H \rightarrow \equiv Si\cdot + H\cdot \qquad (2)$$

$$O_2 \xrightarrow{h\nu} 2O\cdot \qquad (3)$$

$$\equiv Si\cdot + O \xrightarrow{h\nu} \equiv Si-O\cdot \qquad (4)$$

レーザー照射後に熱ポーリングすることによって、電子は H 原子から$\equiv$Si-O・に移動し、$\equiv$Si-O と H^+が生成する。すなわち、

$$\equiv Si-O\cdot + H \rightarrow \equiv Si-O + H^+ \qquad (5)$$
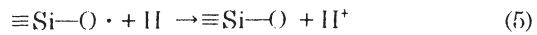
$$poling$$

生成した H^+は印加された電界によって陰極側に移動し、金属電極から供給された電子によって中和される。一方、$\equiv$Si-O は O 原子によって3方が固定されているためそのまま動かないため、結果として陽極近傍に$\equiv$Si-O が局在する。その結果、陽極近傍に直流電界 Edc が発生し、ガラスが本来持つ$\chi^{(3)}$とあわさって$\chi^{(2)}$が発生する（$\chi^{(2)} \propto \chi^{(3)} \times E_{dc}$）と結論できる。

次に1度作成した試料に再度 KrF エキシマレーザーを照射すると$\chi^{(2)}$が消去するメカニズムについて考察する。KrF エキシマレーザーのフォトンエネルギー(約 5eV)は、$\equiv$Si-O の吸収ピーク (4.8eV)にほぼ等しく、照射により波長 650nm の蛍光を呈する。図3にその蛍光の発生過程を示す。$\equiv$Si-O が KrF エキシマレーザーのフォトンを吸収し、エネルギー移動が起こって$\equiv$Si-O*を介して蛍光がおこる。赤色蛍光強度も照射に対して、$\chi_{33}^{(2)}$の減少とほぼ同様の傾向を示したことはとりもなおさず、$\equiv$Si-O の減少が$\chi^{(2)}$の減少に寄与していることを明確に示している。

以上の結果より$\equiv$Si-O が2次非線型光学性発現に関係していると結論付けることができる。

5 まとめ

今回、我々は純粋石英ガラス（ただし O_2 分子と OH を有する）に熱ポーリングに先駆け KrF エキシマレーザーを照射することにより、大きな2次非線形光学性を発現することを見いだした。また一度生成した2次非線形光学性は再度 KrF エキシマレーザーを照射することにより効率よく消失し、消去過程は1光子過程であった。さらに照射の際、1.9eV の赤色の蛍光強度が$\chi^{(2)}$の値と同様に減少した。2次非線形光学性は$\equiv$Si-O によって生成した直流電界 Edc とガラスが本来持っている$\chi^{(3)}$と合わさって発現したものである（$\chi^{(2)} \propto \chi^{(3)} \times E_{dc}$）と結論できる。

6 参考文献

1) R.A.Myers, N.Mukherjee and S.R.J. Brueck. Opt. Lett. 16, 1732 (1991).

2) N.Mukherjee, R.A.Myers and S.R.J. Brueck. J. Opt. Soc. Am. B. 11, 665 (1994).

3) L.J.Henry, A.D.DeVilbiss, and T.E. Tsai, J. Opt. Soc. Am. B. 12, 2037 (1995).

4) T.Fujiwara, M.Takahashi, and A.Ikushima,
   Appl.Phys.Lett. **71**, 1032(1997).

5) P.G.Kazansky, V.Pruneri and P.St.J.Russell, Opt.
   Lett. **20**, 843 (1995).

6) V.Pruneri, G.Bonfrate, P.G.Kazansky, C.Simonneau,
   P.Vidakovic and J.A.Levenson, Appl. Phys. Lett. **77**,
   1998).

7) A.Kameyama, E.Muroi, A.Yokotani, K.Kurosawa and
   P.Herman, J.Opt.Soc.Am. B **14**, 1088 (1997).

8) R.J.Pressley, "Handbook of Lasers with Selected
   Data on Optical Technology", The Chemical Rubber
   Co., Clevel and, Ohio (1972).

9) S.Munekuni, T.Yamanaka, Y.Shimogaichi, R.
   Tohmon, Y.Ohki, K.Nagasawa and Y.Hara J.Appl.
   Phys. **68**, 1212 (1990).

10) F.L.Galeener, D.B.Kerwin, A.J.Miller, and
    J.C.Mikkelsen, Jr., Solid State Commun. **82**,
    271(1992).

11) N.Kuzuu,Y.Matsumoto and M.Murahara Phys.Lev.
    B. **48**, 6952 (1993).

12) N.Kuzuu,Y.Komatsu and M.Murahara Phys.Lev.
    B. **47**, 3078 (1993).

図1 熱ポーリング前に照射した KrF エキシマレーザーのパルス数と誘起された $\chi_{33}^{(2)}$ の関係。● : 熱処理せず。■ : レーザー照射前に空気中で 900℃ で熱処理したもの。

表1 KrF エキシマレーザーを照射してから熱ポーリングした合成石英ガラスの $\chi_{33}^{(2)}$。各雰囲気中での熱処理は 900℃ で2時間行った。

No.	Synthesized condition	Annealing condition	OH contents (ppm)	$\chi_{33}^{(2)}$ (pm/V)
A-1	$H_2/O_2<2$	none	1200	0.51
A-2		in air		0.71
A-3		in He		0.45
B-1	$H_2/O_2>2$	none	1200	0
B-2		in air		0.03
B-3		in He		0.27
C-1	$H_2/O_2>2$	none	550	0
C-2		in air		0
C-3		in He		0

表2 試料(A-1)の $\chi_{33}^{(2)}$ が 1/e になる KrF エキシマレーザーのショット数。

KrF* laser fluence (mJ/cm²)	critical shot number	Product of shot number and fluence
0.6	720	432
6.0	77	462
60.0	8	480

図2 熱ポーリング石英ガラスに KrF エキシマレーザーを照射したときの $\chi_{33}^{(2)}$ の変化と 1.9eV 蛍光強度の変化。● : $\chi_{33}^{(2)}$。■ : 1.9eV 蛍光強度。
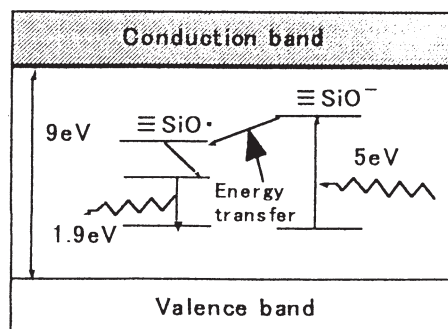
図3 UV 光を照射したときに発生する 1.9eV 蛍光の発生メカニズム

PPMgLNを用いた高平均出力光パラメトリック発振器
High-Average Power optical parametric oscillator based on PPMgLN

山本　修平、平野　嘉仁、谷口　浩一[*]
S.Yamamoto , Y.Hirano , H.Taniguchi[*]

三菱電機株式会社、[*]三菱電線工業株式会社
Mitsubishi Electric Corporation、[*]Mitsubishi Cable Industries, LTD.

Abstract

　We have demonstrated high average power, room temperature operation of PPMgLN OPO.　A high brightness, high repetition rate Q-switched Nd:YAG rod laser was used as a pump laser and the PPMgLN of 1mm-thickness was used for OPO.　Maximum conversion power of 60.2-W with conversion efficiency of 61.1 % was obtained for signal wavelength (1.57μm) and idler wavelength (3.3μm).　For near degenerate OPO, total conversion power of 57-W was obtained with conversion slope efficiency of as high as 82.2 %.

キーワード：レーザ、全固体レーザ、Nd:YAG、光パラメトリック発振器、PPLN、PPMgLN
(Lasers, All solid state lasers, Nd:YAG, OPO, PPLN, PPMgLN)

1．はじめに

　高出力で、広帯域波長可変の近・中赤外レーザの実現は分光計測、光化学反応、IRCMなど多くの応用に期待されている。このような光源の実現手段として、広帯域の利得を有するレーザ媒質を用いたレーザや、固体レーザや半導体レーザなどを励起光源とした光パラメトリック発振器（OPO : Optical Parametric Oscillator）が挙げられる。特に、固体レーザの中で最も高性能化が進んでいる1μm帯のLD励起固体レーザを励起光源としたOPOは、出力、効率、ビーム品質などの点から最も期待されている方式である。OPOによる高出力、高効率な波長変換を考えた場合、励起光源としての固体レーザには、偏光出力で、高輝度であることが求められる。一方、OPOにおける非線型材料には、高出力化を達成するための低損失性と、高効率化に向けて高い非線型定数や長尺結晶の製作性などが求められる。

　本報告では、比較的低パワーにおいて、高い変換効率が実現されている疑似位相整合（QPM：Quasi-Phase Matching）デバイスである周期的分極反転ニオブ酸リチウム（PPLN : Periodically Poled LiNbO₃）と、高輝度のNd:YAGレーザを組み合わせることで、高出力OPOについて実験的な検証を行い、PPLN-OPOの高出力・高効率動作を実証したので、その結果について述べる。

2．高効率・高出力化の課題

　疑似位相整合デバイスは、バルク型に比べ、高い非線形性を有すること、ウオークオフが無いことなどから高効率波長変換に適している。特にPPLNは、高い実効的非線形定数（>15pm/V）、広い透過波長範囲（0.32〜5μm）を有するとともに、長尺結晶（〜50mm）が生成可能であ

るなどの理由から得に高効率化に有利であり、これまで多くの高効率波長変換の事例が報告されてきた。しかし、これらのPPLNを用いたOPOにおいての、最大平均出力は10W以下に抑えられている[1, 2, 3]。この理由として、素子の厚みが薄いため（＜1mm）、レーザ光のパワー密度が高くなることから、素子の損傷しきい値により最大出力が規定されること、副次的に発生する可視光によりフォトリフラクティブダメージが発生することなどが挙げられる。このため、これまで高出力動作OPOとしては、バルク結晶を用いたものが主流であり、6個のKTPを用いたOPOで53Wの出力を43%の変換効率で得た報告[4]や、4個のKTAを用いたOPOで33Wの出力を31%の変換効率で得た報告[5]などがあるが、PPLNなどの疑似位相整合デバイスを用いた例は報告されておらず、高効率・高出力の同時実証はなされてこなかった。

3．高平均出力光パラメトリック発振の実証

　上記の課題を解決し、PPLNにより高効率・高出力を同時達成する一つの方法として、励起光の単一パルス当たりのピークパワー密度を破壊しきい値以下に抑え、パルス繰り返し数を増加させることで平均出力の増大を図ることが有効であると考えられる。また、フォトリフラクティブダメージに対しては、PPLNを高温度保持することや、MgO添加PPLN (PPMgLN)[6]を用いることで、その発生を抑えることが可能である。特にPPMgLNはPPLNと同等の非線形定数、透過波長域、破壊しきい値等を持ち、室温動作においてもフォトリフラクティブダメージが起こらないことが知られており、高出力化には非常に有効な材料である。

　これらの観点から、我々は、平均出力を一定に保ったままパルス繰り返し数により1パルス当たりのエネルギーを制御可能な高輝度・QスイッチNd:YAGロッドレーザを開

発するとともに、PPMgLN-OPOを組み合わせることで、高平均出力で高効率なOPOの動作が可能と考え、OPO変換波長として1.5μm帯、3μm帯の動作、および、変換波長2μm帯の縮退近傍での動作について実証試験を行った。

3．1　励起用固体レーザ

PPLN等の小開口で長尺の波長変換素子の励起では、小ビーム径で長いコンフォーカル長が得られる高輝度な励起ビームを用いることが有効である。また、波長変換出力の高輝度化の観点からも、励起光は高輝度であることが望ましい。

我々は、これまで高輝度な励起光源の開発を行っており、すでに、ほぼ回折限界ビームを発生する高輝度QスイッチNd:YAGロッドレーザについて報告を行っている。ここでは、このレーザの共振器内に偏光子を挿入することで、直線偏光の高輝度Qスイッチパルスの発生を行った。図1にレーザの構成を示す。低熱収差ロッドを実現するための均一ロッド励起方式[7]（HiDiCAD: Highly Diffused Cross-Axis Pump Delivery System）、有効に熱複屈折補償および熱複レンズ補償を実現するための、対称型共振器構成と間に90度旋光子を挿入した2ロッド構成[8]、安定発振領域を励起最大出力にシフトさせる熱レンズ補償用レンズが特長である[8]。レーザロッドはϕ3mmの小径ロッドを用いており、共振器は長さ0.67mの対称型である。Qスイッチは、スイッチングの高速化、消光比の向上のために、音響光学素子2台で構成し、高効率と短パルス化を図るために疑似CW励起（25% duty）と高速のQスイッチングを組み合わせたバーストモードQスイッチ方式[9]を採用している。図2に励起平均出力1.01kWにおけるレーザの平均出力とパルス幅のQスイッチング繰返し依存性を示す。Qスイッチ繰返し数50～160kHz（25% duty、12～40kpps）の全領域において平均出力はほぼ160Wと一定であり、ビーム品質は全ての範囲においてM[2]=1.1である。繰返し数を選択することでパルス幅は34～100nsecまで変えることができ、これによりパルスピークパワーを40kW～376kWまで可変できる。図3に最大出力時のビームプロファイルを示す。良好なガウシアン形状が得られている。

3．2　高平均出力OPO波長変換試験
3．2．1　構成

図4に高平均出力OPOの試験構成を示す。励起光としては、Nd:YAGレーザからの出力を出力可変用のアッティネータにより調整して用い、レンズによりビーム径を調整して温度調整器により温度制御を行っているPPMgLNに入射させた。PPMgLNは、MgOが5 mol%添加のコングルーエント組成MgO:LNから製作しており、入射開口と作用長は、それぞれ1"×1"mm、29mm[L]、反転周期Λは30.8μmで
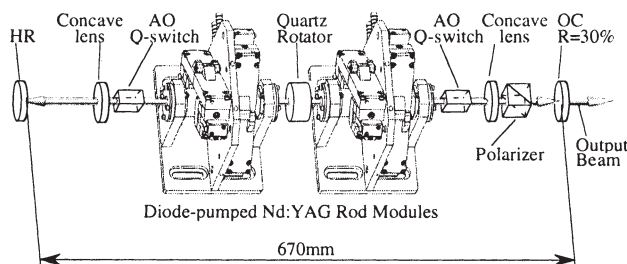
図1　高輝度・QスイッチNd:YAGロッドレーザの構成
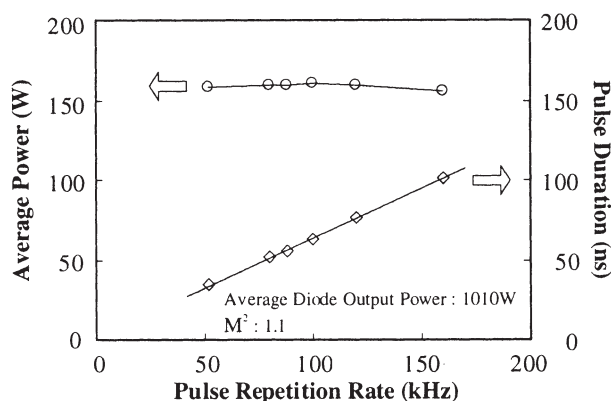
図2　発振出力とパルス幅のパルス繰返し依存性
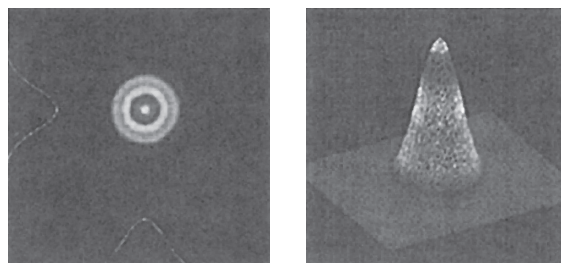
図3　Nd:YAGロッドレーザのビームプロファイル
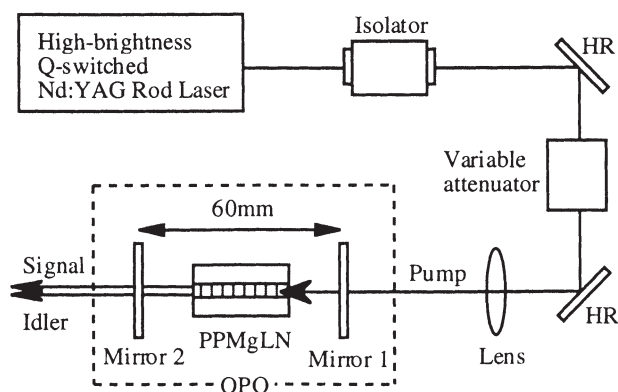
図4　PPMgLN-OPO実験系

ある。OPOは励起光を出力鏡（Mirror 2）で反射させるダブルパス励起であり、励起光入射側共振鏡（Mirror 1）の反射率が励起光（1.064μm）、シグナル光（1.57μm）、アイドラ光（3.3μm）に対して、それぞれ、R<2%、R=99%、R=20%、出力鏡（Mirror 2）の反射率がそれぞれ、R>99%、R=40%、R=10%のSRO（Singly Resonant Oscillator）構成である。キャビティー長は60mmとし、発振しきい値近傍において、励起光と共振シグナル光のモード結合が最適になるように設定している。この構成において、励起光入射側共振鏡（Mirror 1）から出力しているアイドラ成分も存在するが、今回、出力鏡（Mirror 2）からのシグナル光およびアイドラ光出力のみを測定している。

　今回製作したPPMgLNの入射開口は 1 mm[□]であるが、透過波面収差の測定から、透過波面収差を低く抑える場合の有効開口は約0.8mmである。このため励起ビーム径は φ 0.55mmとした。

３．２．２　出力特性

　図 5 にOPO出力の励起光平均出力依存性を示す。励起光のパルス繰返し数は120kHz（25% duty、30kpps）、パルス幅は73nsecである。励起光平均出力98.6Wのとき、シグナル光（1.57μm）およびアイドラ光（3.3μm）の出力はそれぞれ43.1W、17.1Wであり、合計のOPO出力として、これまでのOPOに対する報告として最大となる平均出力60.2Wを得た。シグナル光およびアイドラ光の波長変換スロープ効率は、それぞれ、49.0%、18.1%、全出力に対するスロープ効率は67.1%である。

　図 6 に波長変換効率のしきい値で規格化した励起光ピークパワー密度依存性を示す。近似曲線から得られる最大の波長変換効率は、励起出力がしきい値の12.3倍の時に64.0%であった。最大の波長変換効率の95%以上が得られる範囲は、しきい値の6〜25倍と広範囲であり、最大出力時の波長変換効率は61.1%である。最大出力時の励起光ピークパワー密度は42MW/cm²、共振光のピークパワー密度と合計で88MW/cm²まで上昇していると考えられるが、室温動作に係わらず、フォトリフラクティブ効果による結晶の劣化は観測されていない。高出力励起時の効率劣化はシグナル光とアイドラ光から 1 μm励起光への逆変換によるものである。

　OPOを出力したシグナル光をレンズで集光し、焦点前後のビーム径をサーマルイメージャーで測定することにより、出力ビームのM²値を測定した。図 7 にシグナル光平均出力が10、20、30Wのときの集光特性を示す。シグナル光平均出力が10WレベルではM²〜1.5と高ビーム品質であるが、高出力になるにしたがいビーム品質は劣化しており、20W出力ではM²=2.8、30W出力ではM²=3.3、最大出力時にはM²〜4 程度となった。一方、出力ビームのファーフィールドパターンはガウス分布であることから、TEM₀₀モードが選択されてはいるものの、ガウシアン
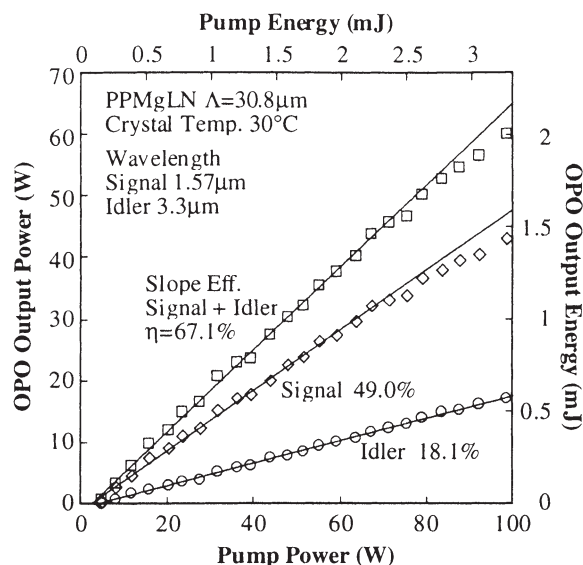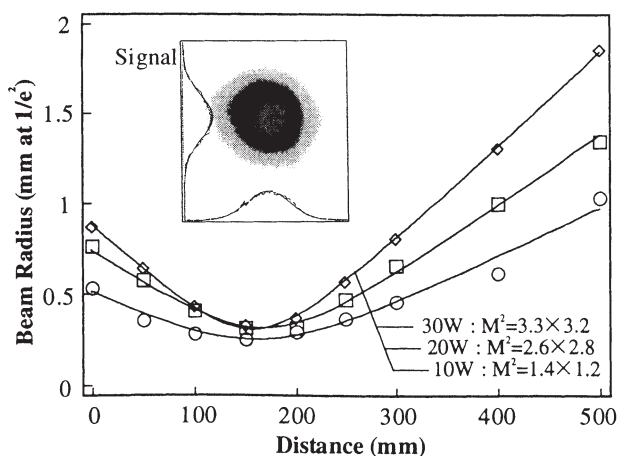

図 5　PPMgLN-OPO出力特性
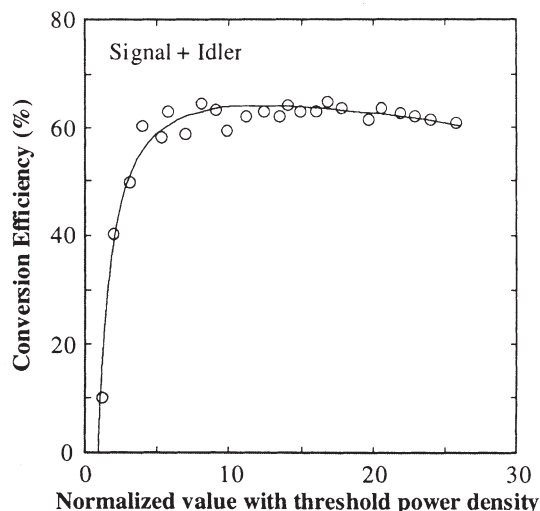
図 6　波長変換効率の励起出力依存性

図 7　シグナルのビーム品質測定結果

ビーム励起に伴う光吸収により発生するPPMgLN内の波面収差が増加することにより、ビーム品質が劣化しているものと考えられる。

３．３　縮退近傍動作による高効率化の実証

OPOを縮退近傍で動作させる構成により、前節で述べた高出力OPOの実証試験におけるアイドラ成分の入射側への漏れによる損失の低減と、OPOの励起光復路パスにおけるシグナル光、アイドラ光のパワー密度を出力結合により低下させることでの逆変換の抑制により、効率の改善を図った。さらに、温度による波長同調試験を行い、広帯域波長掃引の検証を行った。

３．３．１　構成

室温近傍で縮退近傍出力の動作を行うために、PPMgLNとして入射開口と作用長は、1'×1.5"mm、30mm$^{\text{L}}$ 反転周期がΛ=32.2μmのものを用いた。OPOにおける励起光入射側共振鏡（Mirror 1）の反射率は、励起光（1.064μm）、OPO出力光（2.13±0.2μm）に対し、それぞれ、R=1.3%、R>98%であり、出力鏡（Mirror 2）の反射率は励起光、OPO出力光に対し、それぞれ、R=99%、R=25〜38%である。本構成においてもダブルパス励起としている。

３．３．２　出力特性

図 8 に縮退近傍動作PPMgLN-OPOの入出力特性を示す。励起光平均出力79.6Wのとき、シグナル光（2.02μm）およびアイドラ光（2.25μm）の平均出力の合計として57Wを得た。波長変換のスロープ効率は、82.2%と前節の結果に比べ高効率が実証できた。

図 9 にOPOへの入射励起光とOPOをダブルパスした後のデプレッション励起光のパルス時間波形を示す。入射励起光とデプレッション励起光の差が共振器内で波長変換されたものである。入射励起光の平均パワーを増加させてもデプレッション励起光の顕著な増加はみられず、逆変換が顕著には起こっていないことがわかる。最大出力近傍での励起光デプレッション率は90%と高い値を維持している（図 9 (c)〜(d)）。

図10にデプレッション率と波長変換効率のしきい値で規格化した励起ピークパワー密度依存性を示す。デプレッション率は、しきい値の約6〜10倍で約90%と高く、同様に波長変換効率は、この領域で約70%を得ている。デプレッション率に対する波長変換効率の割合は比較的全領域で約80%であるため、波長変換した光の内、約80%が出力として取り出され、約20%が共振損失になっていると考えられる。

図11に出力10Wレベルでの縮退近傍の温度同調試験結果を示す。高平均出力動作試験で用いた反転周期Λ=32.2μmでは、結晶温度が約68℃でほぼ縮退条件となり、20℃から48℃の変化で、1.85〜2.5μmまでの連続的な
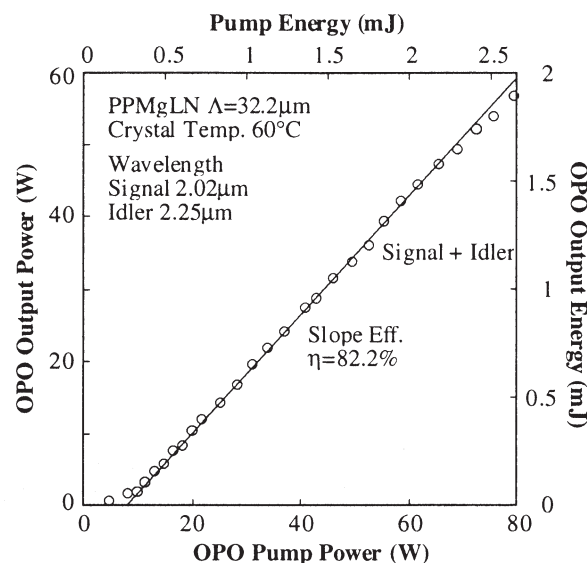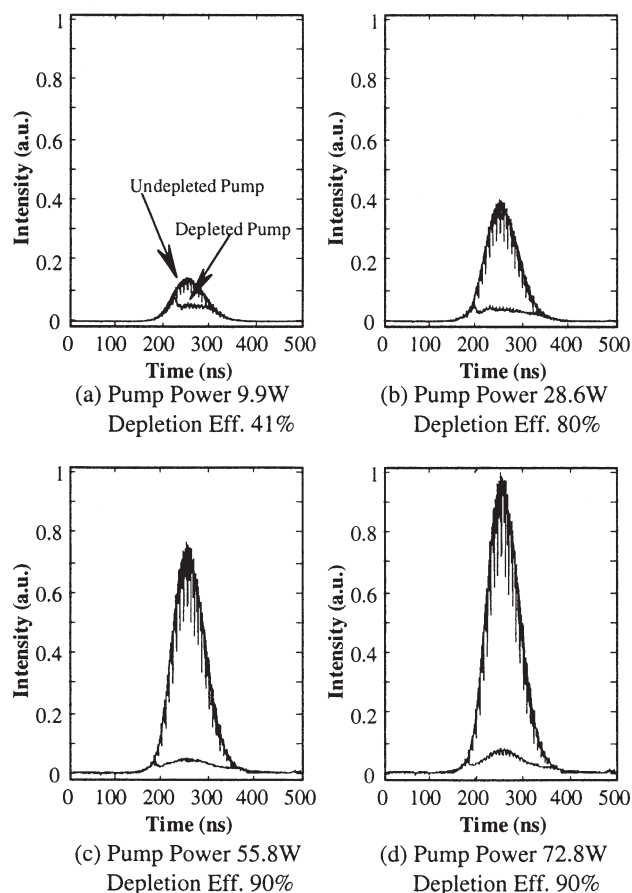

図 8　縮退近傍動作PPMgLN-OPOの出力特性

図 9　励起光とデプレッション光の時間波形

波長掃引が可能であった。また、反転周期Λ=32.3μmの
PPMgLNでは、より室温近傍で縮退条件を作ることができ
た。図11に示した計算値は、文献10に示されている
LiNbO$_3$のセルマイアー方程式を用いフィッテングにより
A$_1$係数のみを4.582→4.785に変えて計算した温度同調特性
である。発振出力の波長の広がりは、シグナル光の場
合、1.57μm出力では半値全幅で0.5nm程度であったが、縮
退に近づくにつれて広がっており、1.85μm出力では6nm、
2μm出力では16nm程度と広がっていることが分かった。
図12に縮退近傍動作における発振波長のスペクトルを示
す。68℃で中心波長が重なっており縮退動作しているこ
とが分かる。

４．まとめ

　偏光出力で高輝度のQスイッチNd:YAGロッドレーザと
PPMgLNを用いたOPOを用いることで、高出力、高効率で
波長可変の赤外光発生の実証を行った。1.5μm、3.3μm出
力では、シグナル光とアイドラ光合計のOPO平均出力と
して60.2Wを61.1%の変換効率で得た。さらに、逆変換抑
制と、アイドラー光損失の低減を図り、縮退近傍の動作
により平均出力57Wで波長変換効率71.4%、スロープ効率
82.2%の高出力・高効率を同時に達成した。また、縮退近
傍動作において、変換波長の温度同調試験を行い、48℃
の温度掃引によりシグナル光に対し0.28μm、アイドラー
光に対し0.37μmの連続波長掃引を実証した。
　今後の課題は、高出力発生時におけるビーム品質劣化
の改善と、発生波長の長波長化である。

参考文献
1. L.E.Myers, et. al., JOSA B, **12**, 2102 (1995).
2. M. E. Dearborn, K. Hoch, and G. T. Moore, Opt. Lett., **23**,759 (1998).
3. 佐久間他, 第59回応用物理学会学術講演会講演予行集, 17a-V-10 (1998).
4. M. S. Webb, G. A. Rines, H. H. Zenzie, and P. F. Moulton, PostDeadline Papers of CLEO'97 Conference, CPD28 (1997).
5. E. Cheung, S.Palese, H.Injeyan, C. Hoefer, R. Hilyard, H. Komine, and J.Berg, Proceedings of ASSL'99 Conference, WC1 (1999).
6. D. A. Bryan, R. Gerson, and H. E. Tomaschke, Appl. Phys. Lett. **44**, 847 (1984).
7. N. Pavel, Y. Hirano, S. Tamamoto, Y. Koyara, and T. Tajime, Appl. Opt., **39**, 986 (2000).
8. Y. Hirano, Y. Koyata, S. Yamamoto, K. Kasahara, and T. Tajime, Opt. Lett., **24**, 679 (1999).
9. Y. Hirano, Y. Koyata, S. Yamamoto, K. Kasahara, in Technical Digest of CLEO'99, paper CMF4 (1999).
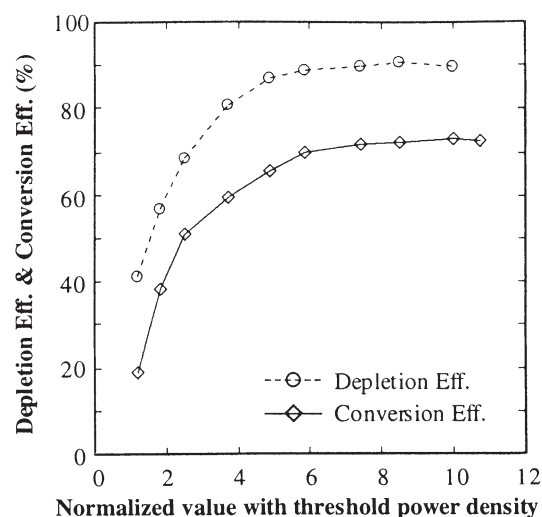10. G.J.EDWARDS, and M. Lawrence, Opt. and Quantum Electron, **16**, 373 (1984).
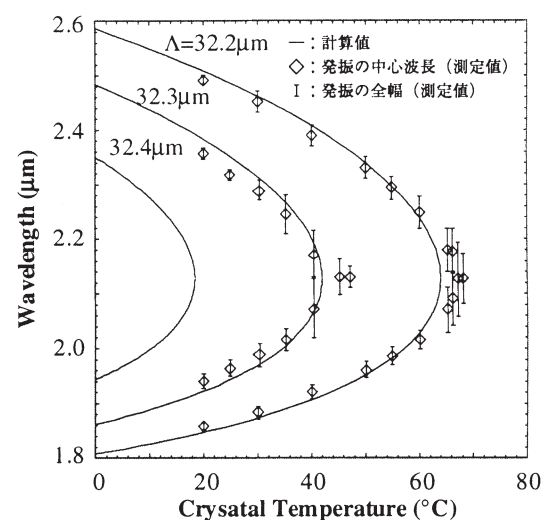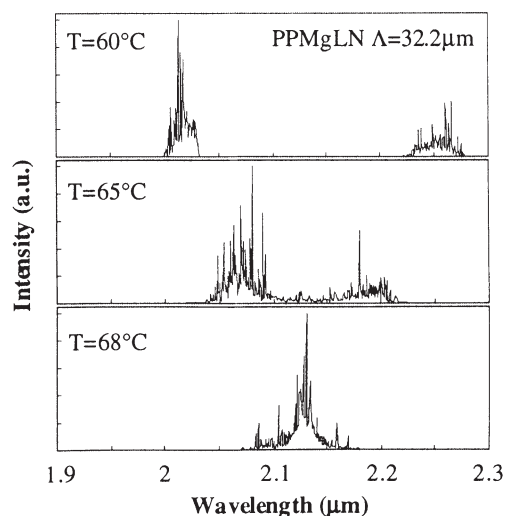
図10　デプレッション率と波長変換効率の
　　　励起出力依存性

図11　温度同調試験結果

図12　発振波長

| 原稿受付日 | 平成 12 年 9 月 27 日 |

Recent Advances in Tunable Terahertz Parametric Generation

* **Hiromasa Ito[1,2], and Kodo Kawase[2]**

[1]Research Institute of Electrical Communication, Tohoku University,
[2]PhotoDynamics Research Center, RIKEN,

Abstract

Spectrum narrowing of a THz-wave parametric generator (TPG) to the Fourier transform limit (v = 1.58 THz, Δv < 200 MHz, Δt = 3.4 ns.) was demonstrated by the introduction of both a single frequency Nd:YAG laser (1.064 μm) as a pump and injection seeding (1.070 μm) of the idler. This resulted in a THz-wave output power (900 pJ/pulse) approximately 300 times higher than that of a conventional TPG, which has no injection seeder. This compact system, which operates at room temperature, promises to be a new THz-wave source for gas tracing, atmosphere monitoring, molecular analysis, etc.

Keywords: THz-wave, parametric generation, nonlinear optics, injection seeding

1. Introduction

Several schemes have been reported for the generation of widely tunable THz-waves in the 1-3 THz region. These include free electron lasers, p-Ge lasers[1], and photo mixing in a photoconductive switch[2]. These techniques suffer from one or more of the following undesirable features: (1) large scale systems, (2) liquid He temperature requirements, (3) tuning throughout the entire tuning range is not possible in one operation, and (4) set up and operational difficulties. In contrast, THz-wave parametric oscillators have proved to be a useful technique for generating continuously tunable THz-waves in 1-3 THz region at room temperature.

We have studied THz-wave parametric oscillators (TPO) and THz-wave parametric generators (TPG) for five years.[3,4,5,6] The main difference between a TPO and a TPG is that a TPO has an idler cavity (near infrared stokes) but a TPG does not. Until recently, the generation of a narrow spectrum THz-wave by a TPG was not expected because a TPG has no frequency selection mechanism. A conventional TPG THz-wave linewidth may exceed 500 GHz. Further, the THz-wave output was much smaller than that from a TPO. Therefore, we have concentrated our efforts on the development of a TPO system that is capable of generating widely tunable THz-waves (1-3 THz, 100-300 μm, 33-100 cm⁻¹, 4.1-12.4 MeV) with a typical linewidth of several tens of GHz.

In this paper, the TPG spectrum was narrowed to the Fourier transform limit of the pulsewidth by introducing both a single frequency Nd:YAG laser and an injection seeder for the idler. At the same time, the obtained THz-wave output was much greater that that from the best TPO available.

2. Experimental setup for an injection seeded TPG

Figure1 shows the experimental setup of an injection seeded TPG. Two nonlinear crystals, $LiNbO_3$ and 5 mol% $MgO:LiNbO_3$, are arranged in series. Three types of arrangement were tested using one, two, and three $LiNbO_3$ crystals. The maximum THz-wave output was obtained when two crystals were used. Although TPG efficiency is higher with $MgO:LiNbO_3$,[7] the crystal quality is low. Therefore, we had to use $LiNbO_3$ for the front side as an idler amplifier. Both crystals were cut into pieces that were 65 × 6 × 5 mm (x × y × z -axis). The x-surfaces at both ends were polished so that they were parallel and coated with antireflection coating centered at 1.064 μm. The y-surface was also mirror polished, in order to minimize the coupling gap between the Si-prism base and the crystal surface. An array of seven Si prism couplers was placed on the y-surface of the $MgO:LiNbO_3$ crystal in order to couple out the THz-wave efficiently.[8] The pump used was an injection seeded single frequency Nd:YAG laser (Spectron SL404T-10, wavelength: 1.064 μm, beam profile:

TEM$_{00}$, energy: < 45 mJ/pulse, pulsewidth: 15 ns, linewidth: ~40 MHz, repetition: 10 Hz, FWHM beam diameter: ~1.4 mmϕ). The pump beam diameter was decreased to 0.8 mmϕ using a telescope in order to increase the power density. The pump power density was < 530 MW/cm^2 at the crystal surface and was varied by an attenuator. The pump beam was almost normal to the crystal surface as it entered the crystals and passed through the MgO:LiNbO$_3$ very close to the y-surface in order to minimize the absorption loss of the THz-wave inside the crystal (α > 10 cm^{-1}). A continuous wave (CW) single frequency Yb fiber laser (IRE-POLUS, YLD-500C-1070, wavelength: 1.070 μm, beam profile: TEM$_{00}$, power: < 300 mW, linewidth: 1MHz, FWHM beam diameter: ~1.3 mmϕ) was used as an injection seeder for the idler.

As shown in the inset of Fig. 1, the THz-wave was generated in a direction that satisfied noncollinear phase matching conditions.[9] Here, k$_j$ is the wave vector with j = p, i, and T, which indicate the pump, idler, and THz-waves, respectively. As the relationship k$_p$ > k$_i$ >> k$_T$ holds, the angle between the pump and idler is small, while the angle between the pump and THz-wave is large. On the outside of the crystal, the angle between the pump and seed beams was almost 1.45° in accordance with noncollinear phasematching conditions. The polarization of the pump and the seed were parallel to the z-axis of the crystals. Thus, an idler (1.070 μm) and a THz-wave (190 μm) were generated simultaneously by injection seeded parametric generation. Idler observation easily confirmed the THz-wave generation. A cylindrical lens (f = 30 mm) made of polymethylpentene (PMP or 'TPX') was used to collimate the THz-wave divergence for the vertical (z-axis) direction. The THz-wave output and temporary waveform were measured with a 4k Si-bolometer (Infrared Laboratories Inc.) and a Schottky barrier diode detector (SBD)[10], respectively. The THz wavelength and the linewidth were measured using a scanning Fabry-Perot etalon consisting of two Ni metal meshes (65 μm grid). The etalon spacing was varied up to 220 mm using a precise actuator. The idler intensity was measured with a power meter and recorded along with the THz-wave output in a computer via a digital oscilloscope.
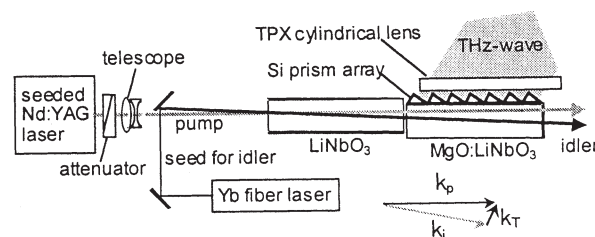

Fig. 1. The experimental setup for an injection-seeded THz-wave parametric generator. The pump was a single mode Q-sw Nd:YAG laser (1.064 μm), and the seed for the idler was a continuous wave Yb fiber laser (1.070 μm). An idler wave (1.070 μm) and a THz-wave (190 μm) were generated simultaneously.

3. Transform-limited, narrow spectrum THz-wave parametric generation by injection seeding

Figure 2 shows the effect of idler spectrum narrowing by injection seeding. The dotted line indicates the idler spectrum of a conventional TPG without injection seeding and the solid line indicates the idler spectrum of an injection-seeded TPG. The resolution limit of the spectrum analyzer was 0.2 nm, so the real idler spectrum was much narrower than this figure. Using a solid etalon, the idler spectrum was assured to be less than 1 GHz.
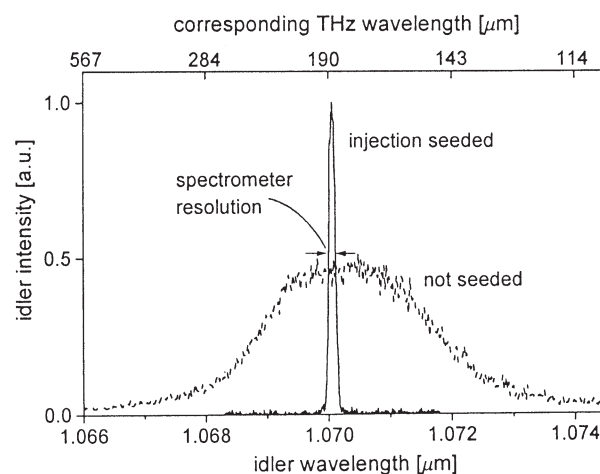

Fig. 2. The narrowing of the idler (1.07 μm) spectrum by injection seeding. The dotted and solid line indicates the idler spectrum of a conventional TPG and an injection-seeded TPG, respectively.

Figure 3 shows the transmitted THz-wave power as a function of the etalon spacing for spacings of ~ 80 mm (a) and ~ 210 mm (b). In this measurement, the incident power of the pump and seed was 40 mJ/pulse and 100 mW, respectively. Figure 3 (a) demonstrates spectrum stability and the displacement between the two periods (190 μm) directly corresponds to the wavelength. The merit of an injection-seeded TPG lies in its mode-hop free characteristic since it has no cavity. On the other hand, in the case of an injection-seeded TPO, the cavity length requires control in order to avoid the mode-hop. In Figure 3 (b), the free spectral range (FSR) of the etalon is 750 MHz and the THz-wave linewidth is measured to be less than 200 MHz (0.0067 cm^{-1}), which is our measurement resolution limit. Since the etalon spacing was up to 210 mm, the number of round trip of the THz-wave pulse (3.4 ns) in the etalon cavity is less than three times; thus, the resolution is inevitably limited. The typical resolution limit of a commercially available FTIR spectrometer in the THz-wave region is around 0.01 cm^{-1}. Therefore, our THz-wave source has sufficient resolution to be used as a spectrometer.

In Figure 4, we calculated the Fourier transform limit of the spectral width from the pulse shape of the THz-wave as measured by SBD. The typical pulsewidth of the THz-wave was 3.4 ns as shown in Fig. 4 (a) and was almost identical to that of the idler, which was measured by a high speed photo detector. Figure 4 (b) shows the power spectrum of the THz-wave calculated from the upper graph, indicating that the linewidth is 136 MHz. In the calculation, we eliminated fluctuations in the background noise at the zero level in Fig. 4 (a). Figures 3 and 4 assured that the linewidth of the THz-wave was narrowed to near the Fourier transform limit. It is very important to note that the THz-wave linewidth is normally > 500 GHz for a conventional TPG using a multi-frequency Nd:YAG laser as a pump. The linewidth still had an ~20 GHz linewidth even with the use of an injection seeded TPG that used a multi frequency mode Nd:YAG laser as the pump.[11] Thus, both the single frequency Nd:YAG laser and the idler seed must be introduced to a TPG in order to obtain the transform limited THz-wave.
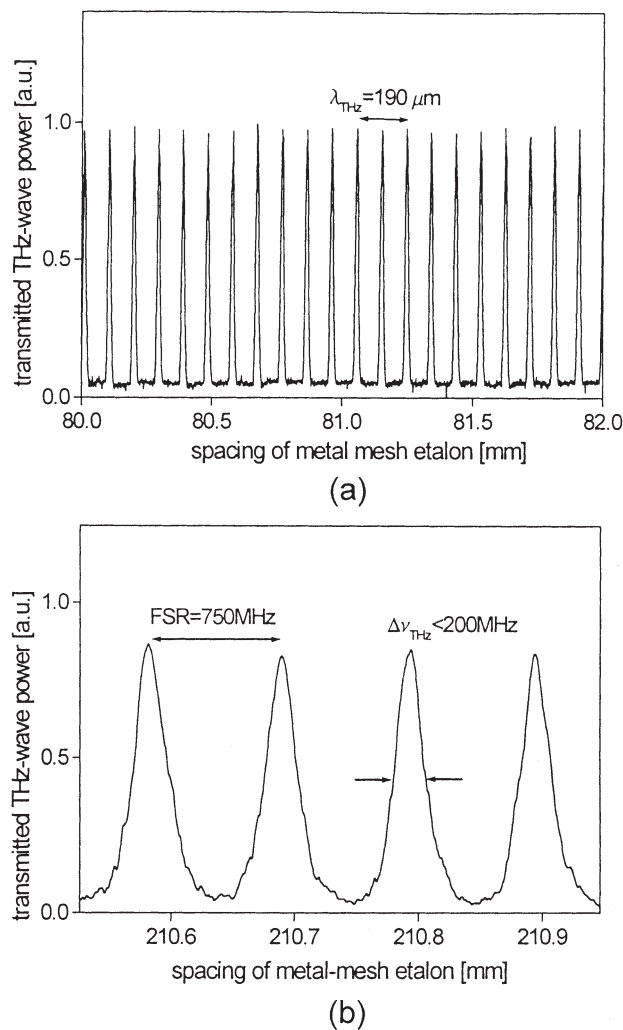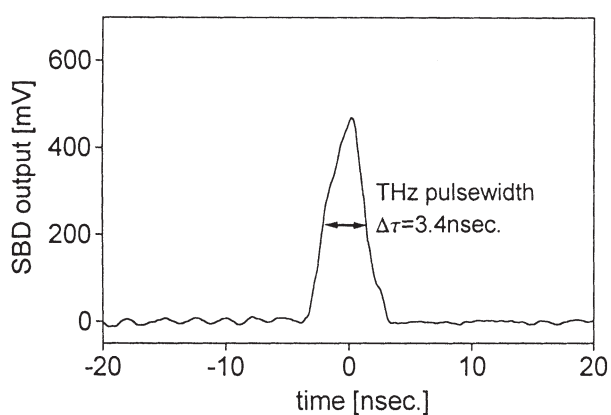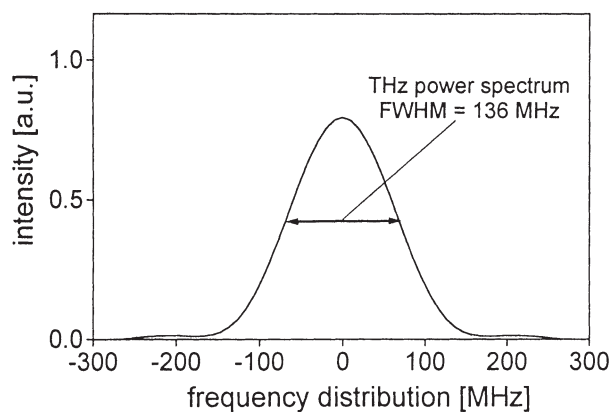

(a)

(b)

Fig. 3. The measured linewidth and wavelength using a scanning Fabry-Perot etalon consisting of two metal mesh plates. (a) The stability of the spectrum is demonstrated and the displacement between the two periods (190 μm) corresponds directly to the wavelength. (b) The FSR of the etalon is 750 MHz and the linewidth of the THz-wave is measured to be less than 200 MHz (0.0067 cm^{-1}), which is our measurement resolution limit.

Figure 5 indicates the change in THz-wave output as a function of the seed incident angle. The seed wavelength (1.07 μm) and generated THz-wavelength (190 μm) were both confirmed as constant. The most effective incident angle was 1.43°, which is the noncollinear phasematched condition. It is

important that injection seeding be effective at the incident angle deviated from 1.43°. We confirmed that the linewidth was also less than 200MHz at the deviated incident angle. The seed incident angle tolerance of 1.2 to 1.7° corresponds to THz-wavelength tuning from 240 to 170 μm, if the seed wavelength is tuned. This suggests that a widely tunable TPG is possible by simply varying the seed wavelength while maintaining a constant seed incident angle. THz-wavelength tuning without mechanical movement will lead to a stable and compact

spectroscopic system. Furthermore, mode-hop free tuning is possible by using a mode-hop free seed source, which is currently under development. In Figure 5, the generated maximum THz-wave power was 400 pJ/pulse as measured by a Si-bolometer with an incident pump and seed power of 40mJ/pulse and 220 mW, respectively.
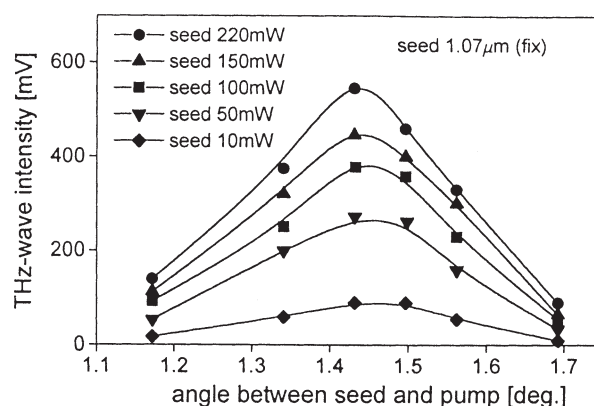
Fig. 5. Variations in THz-wave output as a function of the seed incident angle. The seed wavelength (1.070 μm) and generated THz-wavelength (190 μm) were confirmed constant.

Fig. 4 (a) Temporal THz-wave output measured by the SBD, and (b) calculated Fourier transform limit of the spectral width from the measured temporal THz waveform. The typical pulsewidth of the THz-wave was 3.4 ns, as shown in upper figure, and the calculated linewidth was 136 MHz, as shown in lower figure.

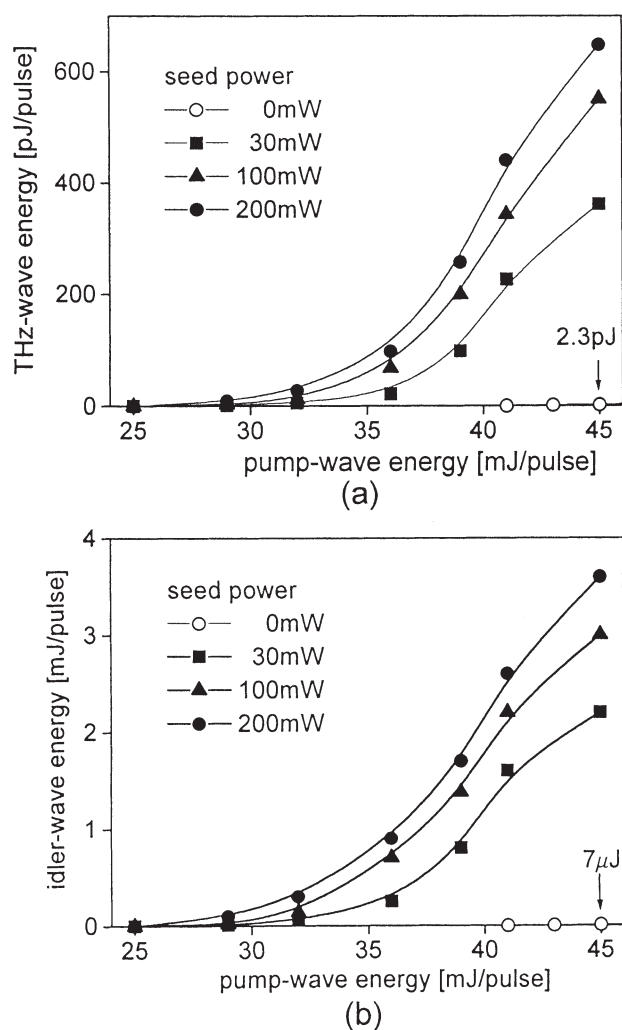## 4. Power enhancement of THz-wave parametric generation by injection seeding

Figure 6 indicates the input-output characteristics of a THz-wave parametric generator. Figure 6 (a) and (b) show the energy enhancement of the THz-wave and the idler, respectively, by injection seeding. It was observed that the THz-wave output and the idler are almost proportional to each other. The THz-wave and idler energy increased almost 300 and 500 times, respectively, by comparing the output at 0 mW and 200 mW seeding. The maximum conversion efficiency was achieved when the pump and seed beams were fully overlapped at the incident surface of the LiNbO$_3$ crystal as shown in Fig. 1, indicating the well known fact that initial excitation is the essential feature of injection seeding.

The maximum THz-wave output of 900 pJ/pulse (peak > 100 mW) was obtained with a pump of 45 mJ/pulse and a seed of 250 mW. In our study, the

records for THz-wave output from a conventional TPG and a TPO were 3 and 190 pJ/pulse, respectively. We had not expected that the output of a seeded TPG exceeded that of a TPO. The Si-bolometer saturated at about 5 pJ/pulse, so we used thick calibrated paper as an attenuator. As the minimum sensitivity of the Si-bolometer was almost 1 fJ/pulse, the dynamic-range of an injection seeded TPG system is 900 pJ / 1 fJ ~ 60 dB, sufficient for most applications. The dynamic-range will be much increased by using lock-in amplifier.

Figure 7 shows the temporal waveforms of the pump, idler, and THz-wave, respectively, using a pump energy of 45 mJ and a seed power of 250 mW. The pulsewidths of the pump and idler are 15 and 4 ns, respectively. This is the largest pump depletion that we discovered during our TPG/TPO research. The THz waveform was found to be depleted, for the first time; this was probably due to the back conversion. Depletion of the THz-waveform was not observed with a pump energy below 35 mJ/pulse. The THz waveform began to deplete as the pump energy increased, although the THz-wave energy continued to increase as shown in Fig. 6 because of the pulsewidth expansion.

Fig. 6. The input-output characteristics of our THz-wave parametric generator (TPG). (a) and (b) show the energy enhancement of the THz-wave and the idler, respectively, with injection seeding.
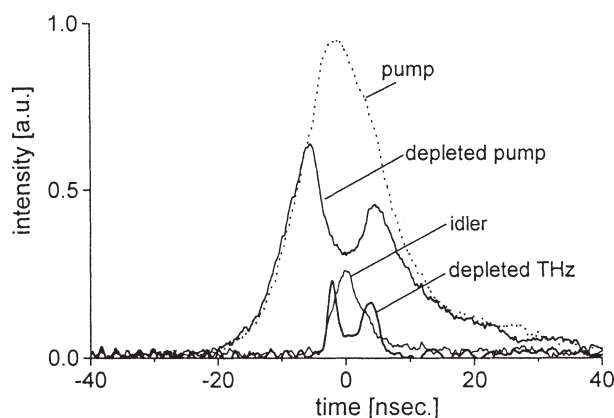

Fig. 7. The temporal waveforms of the incident pump (1.064 μm), depleted pump, non-depleted idler (1.07 μm), and depleted THz-wave (190 μm). The pump energy was 45 mJ and the seed power was 250 mW.

Figure 8 shows the THz-wave beam pattern in the horizontal (upper) and vertical (lower) direction, respectively, at a distance of ~40 cm from the Si-prism array. The beam pattern was nearly Gaussian and had a diameter of 7 mmϕ, which is suitable for many applications. As for the horizontal direction, the beam diameter decreased as it propagated due to the phased array effect of the Si-prism array.[8] The original divergence for the vertical direction was controlled by the pump beam diameter and was about 3°. The cylindrical TPX lens was introduced in order to collimate the vertical divergence as shown in Fig. 1.

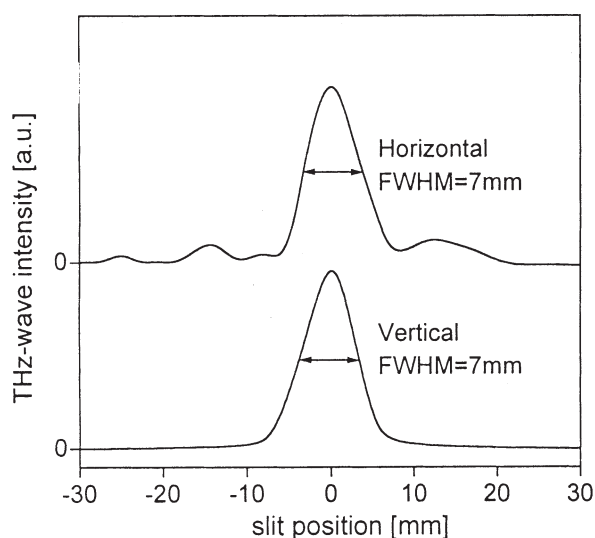Further, the THz beam can be tightly focused using a TPX lens with a shorter focal length.

Fig. 8. The beam pattern of the THz-wave in the horizontal (upper) and vertical (lower) directions, at a distance of ~40 cm from the Si-prism array.

5. Conclusions

In conclusion, we have demonstrated a single frequency and efficient THz-wave parametric generator using an injection seeded single mode Nd:YAG laser as a pump and a Yb fiber laser as an injection seeder for the idler. The linewidth of the generated THz-wave was <200 MHz and approached the Fourier transform limit as decided by the pulsewidth. We also discovered that injection seeding is not overly sensitive to the seed incident angle. This suggests the possibility of a widely tunable THz-wave generator by simply varying the seed wavelength without varying the incident angle. Unfortunately, the injection seeder used in this report was not tunable. We will soon introduce a tunable seeder to our TPG and examine the possibility of wide tunability without varying the incident angle. Success in this will prove the practicality of a new THz-wave source that simply consists of a single mode YAG laser, an injection seeder, and a MgO:LiNbO$_3$ crystal with a prism array. This new source will compete with free-electron and p-Ge lasers.

References

1 E. Brundermann, A. M. Linhart, H. P. Roser, O. D. Dubon, W. L. Hansen, E. E. Haller, Appl. Phys. Lett. 68, 1359 (1996).
2 E. R. Brown, K. A. McIntosh, K. B. Nichols and C. L. Dennis, Appl. Phys. Lett. 66, 285 (1995).
3 K. Kawase, M. Sato, T. Taniuchi, and H. Ito, Appl. Phys. Lett. 68, 2483 (1996).
4 K. Kawase, M. Sato, K. Nakamura, T. Taniuchi, and H. Ito, Appl. Phys. Lett. 71, 753 (1997).
5 J. Shikata, K. Kawase, M. Sato, T. Taniuchi, and H. Ito, Opt. Lett. 24, 202 (1999).
6 K. Kawase et al., Opt. Lett. 24, 1065 (1999).
7 J. Shikata, K. Kawase, K. Karino, T. Taniuchi, and H. Ito, IEEE Trans. Microwave Theory Tech. 48, 653 (2000).
8 K. Kawase, J. Shikata, H. Minamide, K. Imai, and H. Ito, paper accepted by Appl. Opt.
9 M. A. Piestrup, R. N. Fleming, and R. H. Pantell, Appl. Phys. Lett. 26, 418 (1975).
10 T. Nozokido, J. J. Chang, C. M. Mann, T. Suzuki, and K. Mizuno, Int. J. Infrared Millim. Waves 15, 1851 (1994).
11 J. Shikata et al., paper submitted to Opt. Lett.

原稿受付日	平成 12 年 9 月 20 日

謝　　辞

実行委員

藤井正明、平等拓範、栗村　直、庄司一郎、ボイクルペイ、ニコライパベル、
斎川次郎、佐藤庸一、片桐　泉、寺田三和子、市野さとみ

Organizers

Masaaki FUJII, Takunori TAIRA, Sunao KURIMURA, Ichiro SHOJI, Voicu LUPEI,

Nicolaie PAVEL, Jiro SAIKAWA, Yoichi SATO,

Izumi KATAGIRI, Miwako TERADA, and Satomi ICHINO

分子科学研究所　分子制御レーザー開発研究センター

444－8585 岡崎市明大寺町字西郷中 38

TEL :(0564) 55－7480

FAX :(0564) 53－5727

Laser Research Center for Molecular Science, Institute for Molecular Science

38 Nishigonaka, Myodaiji, OKAZAKI, 444－8585　JAPAN

TEL：＋ 81－564－55－7480

FAX：＋ 81－564－53－5727